Doctoral Dissertation (Censored)
博士論文（要約）

Evaluation and Compensation of Betatron Resonances for High-Intensity Proton Synchrotrons

（大強度陽子シンクロトロンにおける ベータトロン共鳴の評価と補正）

A Dissertation Submitted for the Degree of Doctor of Philosophy
December 2020
令和2年12月博士（理学）申請

Department of Physics, Graduate School of Science,
The University of Tokyo
東京大学大学院　理学系研究科
物理学専攻

Takaaki Yasui
安居 孝晃

Abstract

In proton synchrotrons, the beam loss derived from the betatron resonances is one of key issues for stable beam operation. Especially, for the high-intensity beams, the serious effects come from both the sextupole-driven resonances and the space-charge-induced resonances. This dissertation proposes methods to compensate these resonances. They are verified through the simulations and the measurements performed in the main ring synchrotron (MR) of Japan Proton Accelerator Research Complex, which is one of the world-highest beam-intensity proton synchrotrons.

We discussed the main source of the integer resonance in MR, and the effects of the resonance on the beam core. We measured the turn-by-turn transverse beam sizes which grew due to the space-charge-induced resonances. A clear difference of the emittance growth between the structure resonance $\nu_x = 21$ and the nonstructure resonance $\nu_x = 22$ was observed in the measurements. These results showed that the space charge effect was the main source for the resonance $\nu_x = 21$. The measured emittance growth strongly depended on the tune. It gave us the knowledge about the relations between the resonances and the tune spread distribution. The results were well reproduced by the tracking simulation including the space charge effects using a particle-in-cell algorithm.

We developed a novel method to compensate the sextupole-driven third-order structure resonance $\nu_x - 2\nu_y = -21$. The new optics for the compensation makes use of the symmetry of the synchrotron and optimizes the vertical phase advance in the arc section. The compensation was confirmed by the aperture survey simulations and also demonstrated by the three kinds of measurements. The first experiment was the horizontal and vertical coupling measurement derived from the resonance. The coupling was observed only for the optics without the compensation. The second experiment was the beam loss measurements. The beam loss around the resonance was clearly reduced using the optics for the compensation. The third experiment was the Fourier analysis of the dipole oscillation in the transverse planes. We observed the Fourier spectra derived from the resonances, and showed that their peaks were clearly suppressed in the optics for the compensation. The three measurements were consistent with the results of the space charge simulations.

It was revealed that each resonance driving term derived from the space charge effect can be weakened by changing the vertical phase advance in the arc section. This method preserves the original tune, and keeps the straight sections dispersion-free. Through the calculations of the on-resonance conditions, the most influential space-charge-induced resonance to the beam loss was specified as $8\nu_y = 171$ in the present neutrino user operation of MR. It was confirmed by the scan of the vertical phase advance in the arc section. The resonance driving term of the resonance $8\nu_y = 171$ correlated the beam loss during the scan. The advantage of the new optics was also supported by the experiments. The beam loss was reduced about 16% compared to the present optics in the injection period of MR.

Acknowledgements

These PhD studies were not completed without the cooperation of the people around me.

First of all, I would like to express my great appreciation for my supervisor, Prof. Tadashi Koseki. Thank you for giving me a lot of opportunities to participate in the research in J-PARC MR. I am really fortunate that I could feel free to propose and to conduct my studies as I wanted. I am deeply indebted to Prof. Susumu Igarashi. Thank you for always being there to teach me when I needed help, and for supporting my research. I will never forget that you revised my first paper all over, which was finally published in PRAB. I would like to express my sincere gratitude to Dr. Yoichi Sato. It was a great help for my studies that you negotiated and secured the beam time for me. It was really interesting to talk with you about various kinds of ideas to seek for better operation. I am extremely grateful to Prof. Kazuhito Ohmi for the implementation of SCTR and for his extensive understanding about the space charge calculations. Almost all of the calculations and the simulations followed your knowledge. I would like to give a special thanks to Dr. Yoshinori Kurimoto for his discernment that the advantage of the new optics can be explained by the space charge effects. I am obliged to Dr. Tetsushi Shimogawa, Dr. Yuichi Morita, and Mr. Kazuki Miura for making a large amount of magnet patterns. I learned that the present stable control of the power supplies was based on many efforts by the power supply group. I am truly grateful to Dr. Yoshinori Hashimoto for setting up the Inj-MRPM and taking the data by it, Dr. Kenichirou Satou for taking the data by IPM, Mr. Shuichiro Hatakeyama for the instruction about the data taking of BPMs, Prof. Takeshi Toyama for teaching me various kinds of monitor systems, and Mr. Masashi Okada for the setting of intra-bunch feedback system. I realized that the monitors are well tuned from various perspectives to be accurate and precise, and they are indispensable to obtain the exact beam status. I would like to express my appreciation to Dr. Yasuyuki Sugiyama, Dr. Fumihiko Tamura, and Prof. Masahito Yoshii for setting up the RF system and providing me the data of the wall current monitor. I learned a lot from your deep insight into the RF conditions and the beams. I would like to thank Prof. Chihiro Ohmori for giving me an opportunity to visit CERN. It became a precious experience to me. I am grateful to Dr. Junpei Takano for the correction of the closed-orbit distortion. I would like to thank all the people in J-PARC for helping my studies, and for supporting my growth as a scientist.

Last, but not least, I would like to thank my family for their care, support, and encouragement to become a fully qualified scientist.

The author was supported by the MEXT program “Program for Leading Graduate Schools” and the JSPS program “Research Fellowship for Young Scientists”.

Contents

Chapter 1

Introduction

Accelerators are used for various kinds of fields, such as elementary particle physics, nuclear physics, material science, life science, medical science, and industrial applications. They have been developed and specialized according to their purposes. Compared to the other types of accelerators (for example the cyclotron), the synchrotron is often used in high-energy and large-scale facilities.

The designs and the optimizations of the synchrotrons have been studied for the stable beam operations. The synchrotron was first proposed by Oliphant[1], and was realized owing to the discovery of the phase stability by Veksler[2] and McMillan[3]. The first synchrotron was the electron synchrotron constructed by McMillan, which employed the weak focusing as well as cyclotrons in those days. In the weak-focusing synchrotrons, the oscillation amplitudes of the beams were so large that they limited the beam energy. To overcome this problem, the strong-focusing scheme was invented by Christofilos[4], Courant, Livingston, and Snyder[5]. As the strong-focusing proton synchrotron, CERN Proton Synchrotron (CPS) was constructed at CERN in 1959, and Alternating Gradient Synchrotron (AGS) at Brookhaven National Laboratory (BNL) in 1960. These two synchrotrons used the combined-function magnets. In 1953, Kitagaki proposed separated-function design[6], which separated the bending and focusing magnets. It was not only economical in a large synchrotron but also advantageous in terms of the beam tuning. The first synchrotron employing the separated-function design was the Fermilab Main Ring.

Soon after the development of the strong focusing, accelerator physicists found the importance of the effects of the imperfections of the magnets[7]. The imperfections of the magnets in the synchrotron affect the beam periodically, leading to the beam instability known as the resonances. Resonances cause the emittance growth and beam loss. The attempt to understand the resonances through the perturbation theory was published by Schoch[8]. The theory about the resonances was consistently summarized by Guignard[9] for example. Since it was found that strong resonances can be avoided by choosing the proper tunes, the present issue is how to suppress the effects of higher-order resonances derived from nonlinear fields.

In the intensity-frontier synchrotrons which are required by the statistical experiments, the self-field Coulomb potentials of the beams make the discussions complicated. It is called the space charge effect. Since the space charge force depends on the position of the particle, it causes the incoherent tune shift[10, 11]. By the effects of nonlinear components of the space charge potential, it also induces multiple resonances[12]. Since it is difficult to measure the tune spread distribution directly, developing and sophisticating the simulations are necessary for understanding the present operation and for upgrading the synchrotrons.

This dissertation mainly studies the main ring synchrotron (MR)[13] of Japan Proton Accelerator Research Complex (J-PARC)[14], which is one of the world-highest intensity-frontier proton synchrotrons. MR provides high-power proton beams for the neutrino experiments (FX operation) and for the hadron experiments (SX operation). Table 1.1 shows the beam energies, pulse repetition frequencies, intensities, and the powers of the major high-power proton synchrotrons in the world. The number of particles in

one pulse is largest at the FX operation in J-PARC MR. To cope with the strong space charge effects due to the world-highest intensity, MR (and RCS) use second harmonic RF cavities[15, 16] and suppress the maximum line density. For higher beam power, MR plans to shorten the cycling time and upgrade the hardware[17, 18].

Table 1.1: Beam energies, pulse repetition frequencies f_{rep}, pulse intensities, and beam powers of the intensity-frontier proton accelerators[19, 20]

Ring	Institute	Energy [GeV/u]	f_{rep} [Hz]	Particle / pulse	Power [kW]
MR (FX)	J-PARC	30	0.403	2.66×10^{14}	515
MR (SX)	J-PARC	30	0.192	5.95×10^{13}	55
RCS	J-PARC	3	25	4.99×10^{13}	600
MI	FNAL	120	0.75	5.20×10^{13}	750
SPS	CERN	400	0.17	4.59×10^{13}	500
SNS[†]	ORNL	1.4	60	1.04×10^{14}	1400
ISIS	STFC	0.8	40	3.12×10^{13}	160
CSNS	IHEP	1.6	25	1.25×10^{13}	80
PSR[†]	LANL	0.8	20	3.12×10^{13}	80
AGS	BNL	24	0.5	5.20×10^{13}	100

As the beam power increases, the requirement for the beam loss becomes severer, because the beam loss causes the radioactivation of the accelerator components. The beam loss is 0.6% - 1% in the present FX operation in J-PARC MR. They are caused by the effects of the higher-order resonances. This dissertation studies the better beam tuning through the evaluations and the compensations of the resonances due to both external and internal field effects. In this chapter, some basic theories about the accelerator physics and introductions for J-PARC are described. In Chapter 2, the resonant sources for the integer resonances are discussed through some results of measurements and simulations[21]. It indicates the better optimization for the tune in terms of the space charge effects. In Chapter 3, a new method for the compensation of the third-order structure resonance is proposed and is verified. Since this new method only requires a sort of symmetry, it is also applicable to many other synchrotrons. In Chapter 4, the method proposed in Chapter 3 is extended to the space charge effects. It shows that the space-charge-induced resonance can be weakened by the method. It is worth investigating in the synchrotron suffering from the space-charge-induced resonances.

1.1 Basics of Beam Dynamics in a Synchrotron

1.1.1 Transverse Dynamics of a Single Particle

The accelerator physics is an aspect of electromagnetism. Let us start from the Hamiltonian of a charged particle in an electromagnetic field:

$$H = c\sqrt{m^2c^2 + (\boldsymbol{P} - e\boldsymbol{A})} + e\phi. \tag{1.1}$$

Here c is the speed of light, m is the mass of the charged particle, $\boldsymbol{P}$ is the canonical momentum, e is the charge of the particle, $\boldsymbol{A}$ is the vector potential, and ϕ is the scalar potential.

[†]SNS and PSR are accumulator rings. The other ones are synchrotrons.

Particle motions in a circular accelerator are usually understood as deviations from the reference orbit. It is useful to discuss particle motions with the independent variable s, which is the path length along the reference orbit. The coordinate system around the reference orbit is called the Frenet-Serret coordinate system. In this coordinate system, the unit vectors are defined as follows:

$$\hat{s}(s) = \boldsymbol{r}_0'(s), \qquad \hat{x}(s) = -\rho(s)\hat{s}'(s), \qquad \hat{y}(s) = \hat{x} \times \hat{s}. \tag{1.2}$$

The prime $'$ represents the differentiation with respect to s, $\boldsymbol{r}_0$ is the reference orbit, ρ is the radius of curvature.

Using new units, Hamiltonian becomes

$$H = c\sqrt{m^2c^2 + (p_x - eA_x)^2 + \frac{(p_s - eA_s)^2}{(1 + x/\rho)^2} + (p_y - eA_y)^2} + e\phi, \tag{1.3}$$

where

$$p_x = \boldsymbol{P} \cdot \hat{x}, \qquad p_s = (1 + x/\rho)\boldsymbol{P} \cdot \hat{s}, \qquad p_y = \boldsymbol{P} \cdot \hat{y}, \tag{1.4}$$

$$A_x = \boldsymbol{A} \cdot \hat{x}, \qquad A_s = (1 + x/\rho)\boldsymbol{A} \cdot \hat{s}, \qquad A_y = \boldsymbol{A} \cdot \hat{y}. \tag{1.5}$$

To change the independent variable from the time t to the path length s, the new Hamiltonian $\bar{H}(\equiv -p_s)$ is defined. The new Hamiltonian becomes

$$\bar{H} = -\left(1 + \frac{x}{\rho}\right)\sqrt{\frac{(H - e\phi)^2}{c^2} - m^2c^2 - (p_x - eA_x)^2 - (p_y - eA_y)^2} - eA_s \tag{1.6}$$

with $(x, p_x; y, p_y; t, -H)$ as the phase-space coordinates.

Assuming $p_x, p_y \ll |\boldsymbol{P}|$ and neglecting higher-order terms, the transverse equation of motion of an on-momentum particle becomes

$$u'' + K_u(s)u = 0 \qquad (u = x, y), \tag{1.7}$$

where

$$K_x(s) = 1/\rho^2(s) + K_1(s), \qquad K_y(s) = -K_1(s), \tag{1.8}$$

$$K_n(s) \equiv \frac{1}{B\rho}\frac{\mathrm{d}^n B(s)}{\mathrm{d}s^n}. \tag{1.9}$$

Eq. (1.7) is known as Hill's equation. The particle motion around the reference orbit is called betatron motion. In circular accelerators, we can assume the periodic condition as

$$K_u(s) = K_u(s + C), \tag{1.10}$$

where C is the circumference of the accelerator. Using Floquet theory, the simplest Hill's equation (1.7) can be solved as

$$u = \sqrt{2J_u\beta_u(s)}\cos(\psi_u(s) + \xi_u), \tag{1.11}$$

$$\psi_u(s) = \int_{s_0}^{s} \frac{\mathrm{d}s}{\beta_u(s)}, \tag{1.12}$$

where J_u, ξ_u are constants, and s_0 is the reference point. The constant ξ_u depends on s_0. The number of betatron oscillation in one revolution is called tune ν_u, defined as

$$\nu_u \equiv \frac{1}{2\pi}\int_{s}^{s+C} \frac{\mathrm{d}s}{\beta_u(s)}. \tag{1.13}$$

The function β_u is called the betatron function. It is useful for discussing the linear betatron motion to introduce

$$\alpha_u(s) \equiv -\frac{1}{2}\beta_u'(s), \qquad \gamma_u(s) \equiv \frac{1 + \alpha_u^2(s)}{\beta_u(s)}. \tag{1.14}$$

The functions $(\alpha_u, \beta_u, \gamma_u)$ are called Twiss parameters.

1.1.2 Transverse Dynamics of Multi Particles

The Hill's equation (1.7) describes the motion of a single particle. In a real machine, a beam is made of multi particles. The physical quantity of an individual particle can not be observed. The observable values in experiments are the moments of them.

Hereinafter, a moment of a variable λ is written as

$$\langle \lambda \rangle \equiv \iint \lambda f(u,u')\mathrm{d}u\mathrm{d}u', \tag{1.15}$$

where $f(u,u')$ is a distribution function of particles with $\iint f(u,u')\mathrm{d}u\mathrm{d}u' = 1$. Using first and second moments, the root mean square (rms) beam sizes in (u,u') coordinates and the correlation can be defined as

$$\sigma_u^2 = \langle u^2 \rangle - \langle u \rangle^2 , \tag{1.16}$$

$$\sigma_{u'}^2 = \langle u'^2 \rangle - \langle u' \rangle^2 , \tag{1.17}$$

$$\sigma_{uu'} = \langle uu' \rangle - \langle u \rangle \langle u' \rangle . \tag{1.18}$$

It is well known that the emittance defined as

$$\varepsilon_u \equiv \sqrt{\sigma_u^2 \sigma_{u'}^2 - \sigma_{uu'}^2} \tag{1.19}$$

is constant ($\mathrm{d}\varepsilon_u/\mathrm{d}s = 0$) in a linear optics if the beam is not accelerated. There are following relations among the beam sizes, the emittance, and the Twiss parameters:

$$\sigma_u(s) = \sqrt{\varepsilon_u \beta_u(s)}, \qquad \sigma_{u'}(s) = \sqrt{\varepsilon_u \gamma_u(s)}, \qquad \sigma_{uu'}(s) = -\varepsilon_u \alpha_u(s). \tag{1.20}$$

The equation of the beam size, called the envelope equation, can be derived from Hill's equation. Using K_u in Eq. (1.7), the envelope equation can be written as follow:

$$\sigma_u'' + K_u(s)\sigma_u - \frac{\varepsilon_u^2}{\sigma_u^3} = 0. \tag{1.21}$$

1.1.3 Introduction for Betatron Resonance

In some cases, it is helpful to discuss the particle motion in angle-action coordinates. The pseudo-Hamiltonian H corresponding to the Hill's equation (1.7) can be written as

$$H(u,u';s) = \frac{1}{2}u'^2 + \frac{1}{2}K_u(s)u^2. \tag{1.22}$$

Using a generating function

$$F_1(u,\psi_u) = -\frac{u^2}{2\beta_u}(\tan\psi_u - \frac{\beta_u'}{2}), \tag{1.23}$$

the conjugate variables (u,u') are transformed to the new conjugate variables (ψ_u, J_u). The new conjugate momentum J_u is called the action and is written as

$$J_u = \frac{1}{2\beta_u}[u^2 + (\alpha_u u + \beta_u u')^2]. \tag{1.24}$$

The new Hamiltonian $\bar{H}$ becomes

$$\bar{H} = H + \frac{\partial F_1}{\partial s} = \frac{J_u}{\beta_u}. \tag{1.25}$$

Since the new Hamiltonian is independent from ψ_u, the action J_u is invariant ($\mathrm{d}J_u/\mathrm{d}s = 0$).

To make it clear the periodicity of the accelerator, the orbiting angle $\theta = 2\pi s/C$ is introduced, where C is the circumference. Changing the independent variable from s to θ, and using a generating function

$$F_2(\psi_u, \bar{J}_u) = \left(\psi_u - \int_{s_0}^{s} \frac{\mathrm{d}s}{\beta_u} + \nu_u\theta\right)\bar{J}_u, \tag{1.26}$$

the new conjugate coordinates $(\phi_u, \bar{J}_u)$ are

$$\phi_u = \psi_u - \int_{s_0}^{s} \frac{\mathrm{d}s}{\beta_u} + \nu_u\theta, \qquad \bar{J}_u = J_u, \tag{1.27}$$

and the new Hamiltonian $\hat{H}$ is

$$\hat{H} = \frac{C}{2\pi}\bar{H} = \nu_u\bar{J}_u. \tag{1.28}$$

Hereinafter, $\bar{J}_u$ is simplified to J_u, and the non-perturbative Hamiltonian H_0 is defined as

$$H_0 = \nu_{x0}J_x + \nu_{y0}J_y. \tag{1.29}$$

Given that there is a small perturbative potential $U(\phi_x, \phi_y, J_x, J_y; \theta)$ and the Hamiltonian is

$$H = H_0 + U(\phi_x, \phi_y, J_x, J_y; \theta). \tag{1.30}$$

To evaluate the nonlinear effect of U, we separate the linear term from U using Fourier transformation:

$$U(\phi_x, \phi_y, J_x, J_y; \theta) = \tilde{U}_{0,0}(J_x, J_y; \theta) + \sum_{(m_x,m_y)\neq(0,0)} \tilde{U}_{m_x,m_y}(J_x, J_y; \theta)e^{i[m_x\phi_x + m_y\phi_y]}, \tag{1.31}$$

$$\tilde{U}_{m_x,m_y}(J_x, J_y; \theta) = \frac{1}{(2\pi)^2}\iint U(\phi_x, \phi_y, J_x, J_y; \theta)e^{-i[m_x\phi_x + m_y\phi_y]}\mathrm{d}\phi_x\mathrm{d}\phi_y. \tag{1.32}$$

First, let us focus on the linear term and neglect the nonlinear potential $\tilde{U}_{m_x,m_y}$ ($(m_x, m_y) \neq (0,0)$). The equation of motion becomes

$$\frac{\mathrm{d}\phi_u}{\mathrm{d}\theta} = \frac{\partial(H_0 + \tilde{U}_{0,0})}{\partial J_u} = \nu_{u0} + \frac{\partial\tilde{U}_{0,0}}{\partial J_u}. \tag{1.33}$$

The linear tune shift $\Delta\nu_u$ is then,

$$\Delta\nu_u(J_x, J_y) = \frac{1}{2\pi}\oint \frac{\partial\tilde{U}_{0,0}(J_x, J_y; \theta)}{\partial J_u}\mathrm{d}\theta. \tag{1.34}$$

This shows that the tune shift can depend on the action of the particle. The nonlinear potential $\tilde{U}_{m_x,m_y}$ ($(m_x, m_y) \neq (0,0)$) can be expressed by Fourier expansion of θ:

$$\tilde{U}_{m_x,m_y}(J_x, J_y; \theta) = \sum_n \hat{U}_{m_x,m_y,n}e^{-in\theta}, \tag{1.35}$$

$$\hat{U}_{m_x,m_y,n}(J_x, J_y) \equiv \frac{1}{2\pi}\oint \tilde{U}_{m_x,m_y}(J_x, J_y; \theta)e^{in\theta}\mathrm{d}\theta \tag{1.36}$$

The term $\hat{U}_{m_x,m_y,n}$ causes the resonance $m_x\nu_x + m_y\nu_y = n$. When the superperiod of the accelerator is N,

$$\hat{U}_{m_x,m_y,n} = \frac{1}{2\pi}\sum_{k=0}^{N-1}\int_{\theta_0}^{\theta_0+2\pi/N} \tilde{U}_{m_x,m_y}e^{in\theta}e^{in\frac{2\pi k}{N}}\mathrm{d}\theta. \tag{1.37}$$

This means that for resonances with (n mod $N = 0$),

$$\hat{U}_{m_x,m_y,n} = \frac{N}{2\pi}\int_{\theta_0}^{\theta_0+2\pi/N} \tilde{U}_{m_x,m_y} e^{in\theta} \mathrm{d}\theta \equiv N\hat{U}_{m_x,m_y,n,1/N}, \tag{1.38}$$

while for resonances with (n mod $N \neq 0$),

$$\hat{U}_{m_x,m_y,n} = 0. \tag{1.39}$$

The resonance with (n mod $N = 0$) is called the structure resonance. In a real machine, there are some magnet imperfections and they break the periodicity of the accelerator. Magnet imperfections enhance resonances even if (n mod $N \neq 0$). The resonance with (n mod $N \neq 0$) is called the nonstructure resonance.

Suppose that a particle with action $(J_x, J_y) = (J_{xR}, J_{yR})$ is on the resonance $m_x\nu_x + m_y\nu_y = n$, that is

$$m_x(\nu_{x0} + \Delta\nu_x(J_{xR}, J_{yR})) + m_y(\nu_{y0} + \Delta\nu_y(J_{xR}, J_{yR})) = n. \tag{1.40}$$

The Hamiltonian can be approximated as

$$H \simeq H_0 + \tilde{U}_{0,0} + V_{m_x,m_y,n}\cos(m_x\phi_x + m_y\phi_y - n\theta + \xi_{m_x,m_y,n}), \tag{1.41}$$

where

$$V_{m_x,m_y,n} = 2|\hat{U}_{m_x,m_y,n}|, \qquad \xi_{m_x,m_y,n} = \arg\hat{U}_{m_x,m_y,n}. \tag{1.42}$$

If $m_x \neq 0$, applying canonical transformation by using the generating function

$$F_2(\phi_x, \phi_y, J_1, J_2) = (m_x\phi_x + m_y\phi_y - n\theta + \xi_{m_x,m_y,n})J_1 + \phi_y J_2, \tag{1.43}$$

the new canonical coordinates are

$$J_1 = \frac{1}{m_x}J_x, \qquad J_2 = -\frac{m_y}{m_x}J_x + J_y, \tag{1.44}$$

$$\phi_1 = m_x\phi_x + m_y\phi_y - n\theta + \xi_{m_x,m_y,n}, \qquad \phi_2 = \phi_y, \tag{1.45}$$

and the new Hamiltonian $\bar{H}$ is

$$\bar{H} = (m_x\nu_{x0} + m_y\nu_{y0} - n)J_1 + \nu_{y0}J_2 + \tilde{U}_{0,0}(J_1, J_2; \theta) + V_{m_x,m_y,n}(J_1, J_2)\cos\phi_1. \tag{1.46}$$

Since $\partial\bar{H}/\partial\phi_2 = 0$, J_2 is a constant, that is

$$m_x J_y - m_y J_x = \text{constant}. \tag{1.47}$$

Approximating $\tilde{U}_{0,0}$ as[22]

$$\tilde{U}_{0,0}(J_1) \simeq \tilde{U}_{0,0}(J_{1R}) + \left.\frac{\partial\tilde{U}_{0,0}}{\partial J_1}\right|_{J_{1R}}(J_1 - J_{1R}) + \frac{1}{2}\left.\frac{\partial^2\tilde{U}_{0,0}}{\partial J_1^2}\right|_{J_{1R}}(J_1 - J_{1R})^2, \tag{1.48}$$

$$J_{1R} = \frac{1}{m_x}J_{xR}, \tag{1.49}$$

and averaging out the linear potential as[22, 23]

$$\bar{U}_{0,0}(J_1, J_2) = \frac{1}{2\pi}\oint \tilde{U}_{0,0}(J_1, J_2; \theta)\mathrm{d}\theta, \tag{1.50}$$

the Hamiltonian becomes

$$\bar{H} = \frac{1}{2}\left.\frac{\partial^2 \bar{U}_{0,0}}{\partial J_1^2}\right|_{J_{1R}} (J_1 - J_{1R})^2 + V_{m_x,m_y,n}(J_1)\cos\phi_1 + \text{constant} \tag{1.51}$$

$$\simeq \frac{\Lambda}{2}(J_1 - J_{1R})^2 + V_{m_x,m_y,n}(J_{1R})\cos\phi_1 + \text{constant}, \tag{1.52}$$

where

$$\Lambda = \left.\frac{\partial^2 \bar{U}_{0,0}}{\partial J_1^2}\right|_{J_{1R}} = m_x^2 \frac{\partial^2 \bar{U}_{0,0}}{\partial J_x^2} + 2m_x m_y \frac{\partial^2 \bar{U}_{0,0}}{\partial J_x \partial J_y} + m_y^2 \left.\frac{\partial^2 \bar{U}_{0,0}}{\partial J_y^2}\right|_{J_{xR},J_{yR}}. \tag{1.53}$$

Therefore the resonance width is

$$\Delta J_1 = 4\sqrt{\frac{V_{m_x,m_y,n}(J_{1R})}{\Lambda}}. \tag{1.54}$$

1.1.4 Space Charge Effect

Since charged particles are bunched in narrow spaces, the electromagnetic fields made by beams have significant effect on the beams, especially in high-intensity synchrotrons. This is called the space charge effect. The space charge effect is often classified into the direct effect and the indirect effect. The former is the Coulomb scattering between particles, and the latter is the effects derived from existence of the walls of the vacuum chambers, such as the mirror charge effect. In this section we neglect the effect through the wall, and we assume that the transverse distribution of the beam is a Gaussian. The space charge potential of the Gaussian beam is[24]

$$U(x,y;s) = \frac{\lambda r_0}{\gamma_{\text{rel}}^3 \beta_{\text{rel}}^2}\int_0^\infty \mathrm{d}q \frac{\exp(-\frac{x^2}{2\sigma_x^2+q} - \frac{y^2}{2\sigma_y^2+q})}{\sqrt{2\sigma_x^2+q}\sqrt{2\sigma_y^2+q}}, \tag{1.55}$$

where λ is the line density of the beam, r_0 is the classical radius of the particle, $\beta_{\text{rel}}, \gamma_{\text{rel}}$ are the Lorentz factors, and σ_u is the rms beam size.

Changing the independent variable from s to θ and transforming the coordinates from (u, u') to (ϕ_u, J_u) by using

$$u = \sqrt{2J_u\beta_u}\cos(\phi_u + \chi_u - \nu_u\theta), \qquad \chi_u(s) = \int_{s_0}^{s}\frac{\mathrm{d}s}{\beta_u}, \tag{1.56}$$

the space charge potential becomes (see Appendix A)

$$U(\phi_x,\phi_y,J_x,J_y;\theta) = \tilde{U}_{0,0} + \sum_{(m_x,m_y)\neq(0,0)}\sum_n \hat{U}_{m_x,m_y,n}e^{i[m_x\phi_x + m_y\phi_y - n\theta]}e^{-i\delta\theta}, \tag{1.57}$$

$$\tilde{U}_{0,0}(J_x,J_y;\theta) = \frac{C}{2\pi}\frac{\lambda r_0}{\gamma_{\text{rel}}^3\beta_{\text{rel}}^2}\int_1^\infty \mathrm{d}\zeta \frac{e^{-w_x-w_y}I_0(w_x)I_0(w_y)}{\sqrt{\zeta^2-\Delta_{xy}^2}}, \tag{1.58}$$

$$\hat{U}_{m_x,m_y,n}(J_x,J_y) = \frac{\lambda r_0}{\gamma_{\text{rel}}^3\beta_{\text{rel}}^2}\frac{(-1)^{(m_x+m_y)/2}}{2\pi}\oint \mathrm{d}s e^{im_x\chi_x + im_y\chi_y} \times \int_1^\infty \mathrm{d}\zeta \frac{e^{-w_x-w_y}I_{m_x/2}(w_x)I_{m_y/2}(w_y)}{\sqrt{\zeta^2-\Delta_{xy}^2}} \qquad (m_u = \text{even}), \tag{1.59}$$

where

$$\delta = m_x \nu_x + m_y \nu_y - n, \tag{1.60}$$

$$\Delta_{xy} = -\Delta_{yx} = \frac{\sigma_x^2 - \sigma_y^2}{\sigma_x^2 + \sigma_y^2}, \tag{1.61}$$

$$w_u = -\frac{J_u \beta_u}{(\sigma_x^2 + \sigma_y^2)(\zeta + \Delta_{uv})} \qquad ((u,v) = (x,y),(y,x)), \tag{1.62}$$

and $I_\nu(z)$ is the modified Bessel function. It shows that the space charge potential makes only even-order resonances.

The linear space charge tune shift is

$$\Delta\nu_u = \frac{1}{2\pi} \oint \frac{\partial \tilde{U}_{0,0}}{\partial J_u} \mathrm{d}\theta \tag{1.63}$$

$$= -\frac{\lambda r_0}{\gamma_{\mathrm{rel}}^3 \beta_{\mathrm{rel}}^2} \frac{1}{2\pi} \oint \mathrm{d}s \frac{\beta_u}{(\sigma_x^2 + \sigma_y^2)} \int_1^\infty \mathrm{d}\zeta \frac{e^{-w_x - w_y}[I_0(w_u) - I_1(w_u)]I_0(w_v)}{(\zeta + \Delta_{uv})^{3/2}(\zeta + \Delta_{vu})^{1/2}}. \tag{1.64}$$

To calculate the space charge potentials and their derivatives, the rms beam size $\sigma_u(s)$ should be solved. It can be obtained from the envelope equation with the space charge effect[25]:

$$\sigma_u'' + K_u \sigma_u - \frac{\varepsilon_u}{\sigma_u^3} - \frac{\lambda r_0}{\beta_{\mathrm{rel}}^2 \gamma_{\mathrm{rel}}^3} \frac{1}{\sigma_x + \sigma_y} = 0. \tag{1.65}$$

This equation holds when the 4-dimensional beam distribution has the elliptical boundary. If the momentum spread $\delta = \mathrm{d}P/P$ of the beam is not negligible, the beam size should be modified as

$$\sigma(s) = \sqrt{\sigma_{\mathrm{transverse}}^2(s) + \sigma_\delta^2 \eta^2(s)}, \tag{1.66}$$

where σ_δ is the rms momentum spread and $\eta(s)$ is the dispersion function.

1.2 J-PARC

1.2.1 Composition of J-PARC

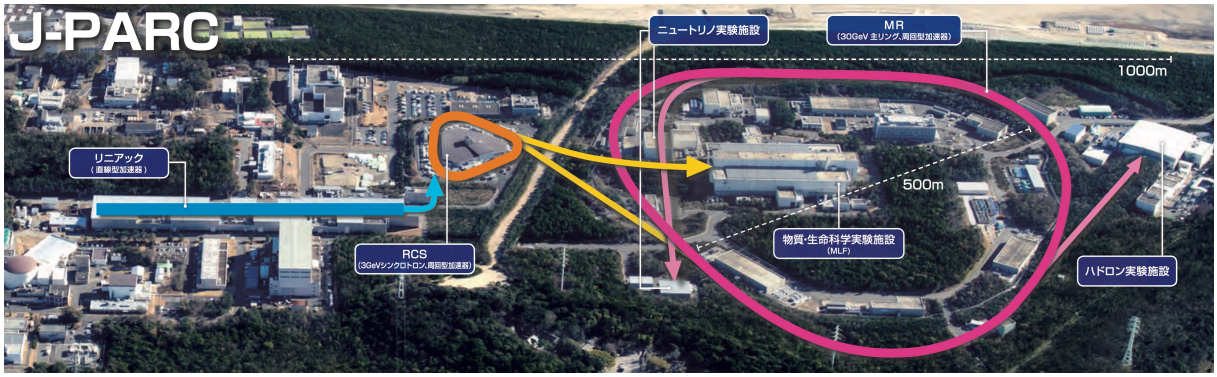

Figure 1.1: Overview of J-PARC[26]

Japan Proton Accelerator Research Complex (J-PARC)[14] is a facility targeting multi-purpose studies using proton beams. Secondary or tertiary particles are made from proton beams, such as neutrons, muons, kaons, neutrinos. The most remarkable specification of J-PARC is the intensity of the beam. High-intensity secondary (or tertiary) beams enable large statistical experiments.

In J-PARC, particles are accelerated up to the relativistic beta $\beta_{\mathrm{rel}} \sim 1$. To keep high acceleration efficiency in each velocity, J-PARC uses three large accelerators.

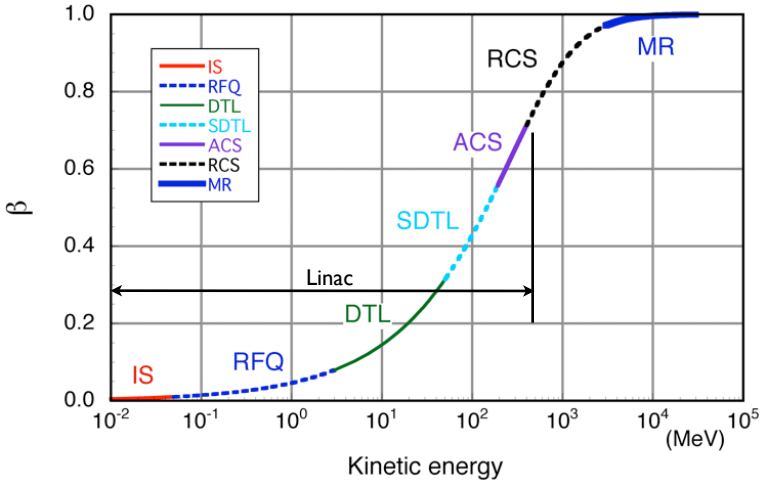

Figure 1.2: Relativistic beta of a proton as a function of the energy[27].

Linac

Linac is the most upstream accelerator in J-PARC, shown as the blue line in Fig. 1.1. Linac consists of IS (Ion Source) and four accelerating structures: RFQ, DTL, SDTL, and ACS. The energy regions of each accelerator are shown in Fig. 1.2. Linac generates H^-s at the Ion Source, and accelerates them up to 400 MeV ($\beta_{\mathrm{rel}} = 0.73$).

RCS

The H^- beams from Linac are injected to 3GeV Rapid Cycle Synchrotron (RCS)[28], shown as the orange line in Fig. 1.1. At the injection, H^-s are converted to protons by the thin carbon foils. RCS operates with 25 Hz. Two beam bunches are accelerated to 3 GeV in one cycle, and extracted to MLF or MR.

MR

30GeV Main Ring Synchrotron (MR)[13] is a proton synchrotron shown as the pink line in Fig. 1.1. Two proton bunches (called a batch) are injected four times at intervals of 40 msec (25 Hz) from RCS. After injection, the beams are accelerated to 30 GeV, and are extracted to Neutrino Experimental Facility or Hadron Experimental Hall.

Experimental Facilities

In Material and Life Science Experimental Facility (MLF), neutrons and muons are made by the nuclear spallation reaction using proton beams injected from RCS. MLF provides Neutron beams and muon beams to various kinds of users.

Neutrino beams are made in Neutrino Experimental Facility using the beams from MR. Neutrinos are detected by the near detector and by the far detector: Super-Kamiokande[29].

Several kinds of hadron beams, such as kaons, pions, and anti-protons, are made in Hadron Experimental Hall by the beam from MR. They are used for nuclear experiments or elementary particle experiments.

1.2.2 Status of MR

Figure 1.3 shows the schematic picture of the main ring synchrotron. The beams from the RCS pass the transport line, called 3-50 BT, and are injected in MR. Eight bunches are injected in total within 0.13 sec,

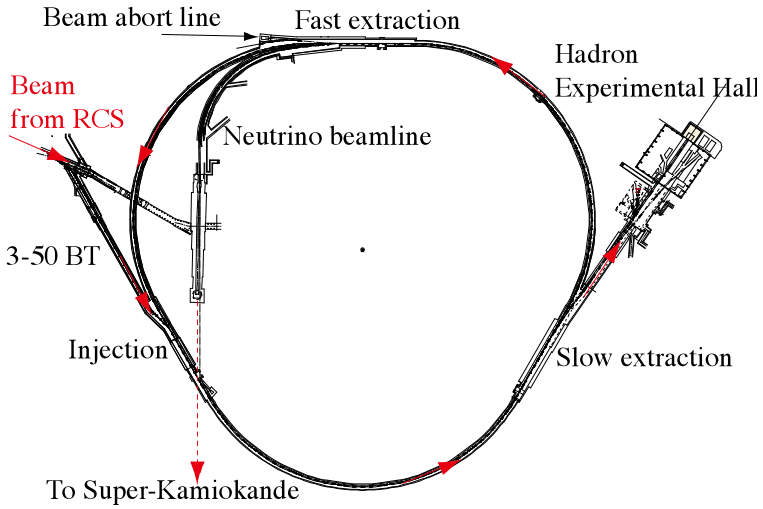

Figure 1.3: Design of J-PARC MR[13]

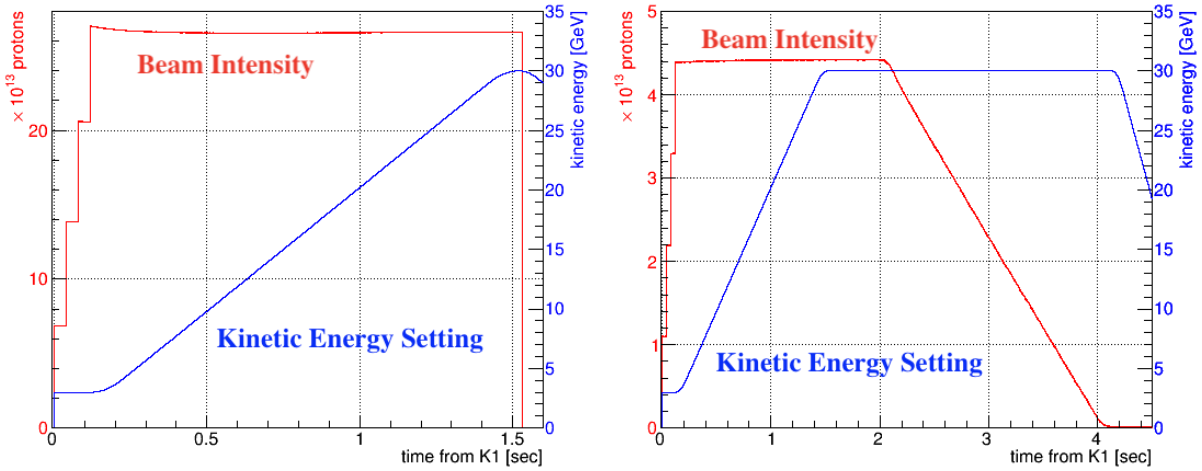

Figure 1.4: An example of the beam intensities measured by the DCCT (red) and the settings of the kinetic energies for the magnets (blue) in FX (left) and in SX (right).

and then they are accelerated from 3 GeV to 30 GeV for 1.4 sec. There are two kinds of extraction modes in MR. One is the fast extraction (FX). FX operation is used for the neutrino experiments[30, 31, 32]. After being accelerated to 30 GeV, all the beams are kicked out in one turn to the neutrino beam line. Then the pion beams are made in collisions between the proton beams and a graphite target, and they decay to muons and muon neutrinos. The other extraction mode is the slow extraction (SX). SX operation is used for the hadron experiments. Since the hadron users require the smooth and uniform beams, the beams are debunched for 0.5 sec after acceleration. Then they are slowly extracted to the Hadron Experimental Hall for 2 sec. The examples of the beam intensities and the settings of the kinetic energies for the magnets are shown in Fig. 1.4. The beam intensity is usually measured by the direct-current current transformers (DCCT)[33, 34, 35, 36] in MR. The cycle time is 2.48 sec in FX and 5.2 sec in SX.

MR comprises three straight sections and three arc sections. Since the beams are injected and extracted at the straight sections, the straight sections are usually called “the insertion sections”. The length of the straight section is 116.1 m, and that of the arc section is 406.4 m. There are seven kinds of quadrupole magnets in the straight sections, and four kinds of quadrupole magnets in the arc sections. The same kinds of quadrupole magnets have the same structures, and their inputs are from the same power supply. We call the group of the same kinds of magnets as a “family”. Since the arc section is

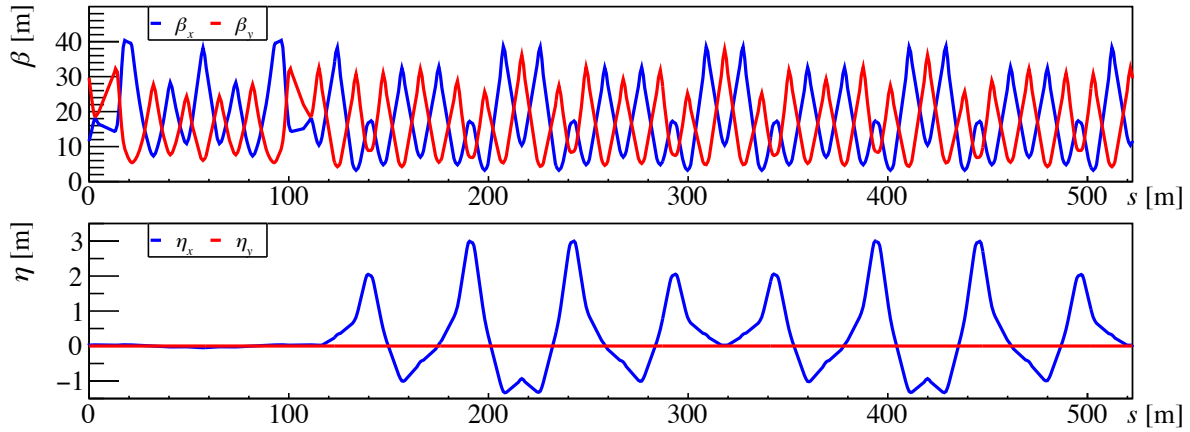

Figure 1.5: The betatron functions (upper) and the dispersion functions (lower) for one superperiod used in the neutrino user operation. The horizontal functions are shown as blue lines, and the vertical ones are shown as red lines.

Table 1.2: The main parameters in MR[13]

Injection energy	3 GeV
Extraction energy	30 GeV
Circumference C	1567.5 m
Harmonic number	9
Number of bunches	8
Superperiod	3
RF frequency	1.67 - 1.72 MHz
Transition energy γ_T	$31.7i$
Physical aperture of the ring	$> 81\pi$ mm mrad
Physical aperture of the collimators	$\sim 60\pi$ mm mrad
Capacity of the collimators	2 kW
Number of the bending magnets	96 (6 families)
Number of the quadrupole magnets (straight section)	45 (7 families)
Number of the quadrupole magnets (arc section)	171 (4 families)
Number of the sextupole magnets	72 (3 families)

much longer than the straight section, the optics parameters, especially the betatron tune, is sensitive to the strength of the quadrupole magnets in the arc sections. The adjustment of the arc sections is also important in terms of the dispersion. The quadrupole magnets in the arc sections are carefully adjusted to make the straight sections dispersion-free. For these reasons, the tune is usually moved by using only the quadrupole magnets in the straight sections if necessary.

The remarkable feature of the lattice of MR is that it employs imaginary transition energy. One arc section is made of eight modules. One module is composed of three FODO cells, and the center of each module is set as the missing-bend cell. The dispersion is set to be positive at the missing-bend cells, and negative at the other arc cells, so that the momentum compaction factor is negative and the transition energy is imaginary. The betatron function and the dispersion for the neutrino user operation is shown in Fig. 1.5. The major parameters of MR are listed in Table 1.2.

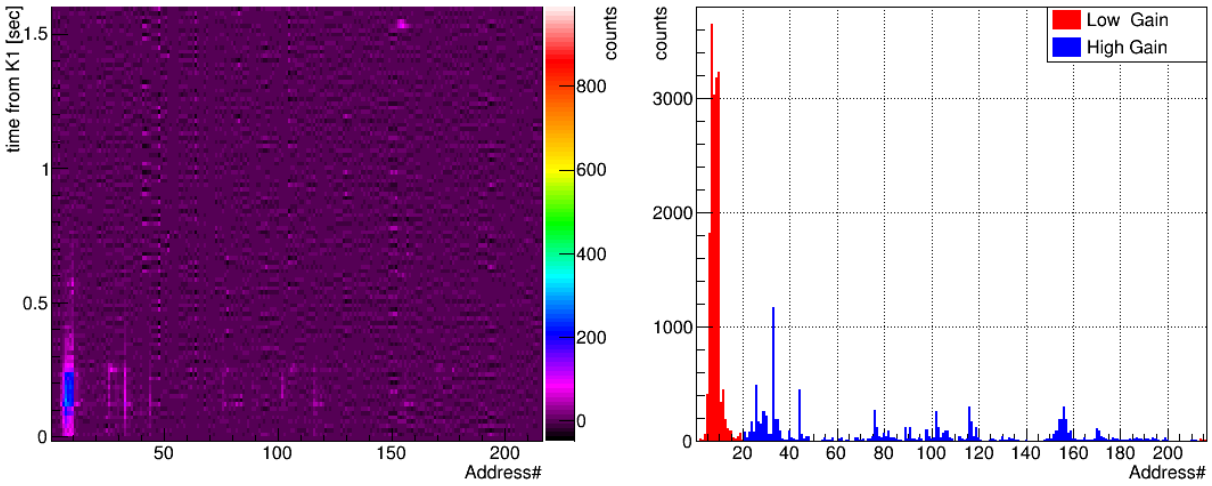

Figure 1.6: Beam loss distributions measured by the proportional counters. The left picture shows an example of the time structure of the beam loss at each position in the neutrino operation. The horizontal axis shows the address, which is the number allocated to the whole of the ring. The vertical axis shows the time. The right picture shows an example of the accumulated beam loss for one shot at each position in the neutrino user operation. The collimator section is colored red, and the other places are colored blue. The gains of the proportional counters at the other places is 8 times as much as those at the collimator section. In other words, if the plot is made with the same gain, the red bars will be 8 times taller.

What is indispensable for the optimization of the high-intensity proton accelerator is control of the beam loss. The lost protons produce a large amount of secondary particles, resulting in the radioactivation of the accelerator components. Serious radioactivation disturbs the maintainability of the accelerator. Since it is impossible to realize the beam operation without any beam loss, the beam loss is localized to some places. Usually, the collimators are installed for the localization of the beam loss. MR is originally designed to secure the physical aperture of 81π mm mrad. The physical apertures of the collimators are typically set about 60π mm mrad to localize the beam loss. Of course the collimators are solidly shielded. It is essential to reduce the total amount of beam losses and to localize them at the collimator sections. Figure 1.6 shows an example of the beam loss distribution measured by the proportional counters[37, 38, 39]. The beam loss is well localized at the collimator section.

Table 1.3: Operation status in MR

	FX	SX
Current beam power	515 kW	55 kW
Design beam power	750 kW	100 kW
Future beam power	1300 kW	100 kW
Current beam intensity	2.66×10^{14} ppp	5.95×10^{13} ppp
Current cycle time	2.48 sec	5.2 sec
Operation Tune (ν_x, ν_y)	(21.35, 21.43)	(22.31, 20.79) (3 GeV)

Since we are searching for the new physics by accumulating the statistics of the neutrinos and the hadrons, MR is requested to increase the beam power. Figure 1.7 shows the history of the beam power in MR. The beam power has been increased by virtue of various kinds of upgrades[40, 41]. One of the efforts which contributed to the beam loss reduction in FX operation was the change of the operation tune[41]. The previous operation tune was (ν_x, ν_y) = (22.40, 20.75) in FX operation. However, the

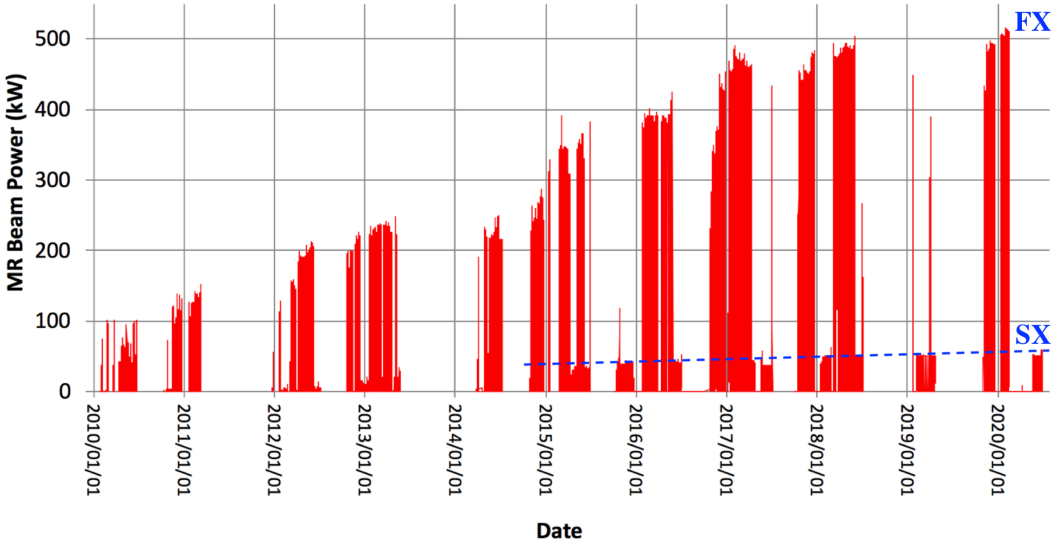

Figure 1.7: The history of the beam power in MR[18]. The high peaks represent the beam power for the FX operation. The low peaks represent the beam power for the SX operation.

resonances, such as $\nu_x + \nu_y = 43$ and $2\nu_y = 43$, limited the beam intensity. The space charge simulation showed the advantage of the tune $(\nu_x, \nu_y) = (21.35, 21.43)$, and encouraged to move the tune[42, 43]. The present operation tune $(\nu_x, \nu_y) = (21.35, 21.43)$ has been applied since May 2016.

The maximum power achieved to 515 kW for the FX operation, and to 55 kW for the SX operation. These powers correspond to 2.66×10^{14} protons per pulse (ppp) or 3.32×10^{13} protons per bunch (ppb) for the FX operation, and to 5.95×10^{13} ppp or 7.44×10^{12} ppb for the SX operation. The operation status of MR is listed in Table 1.3.

1.2.3 Future Plan and Issues in MR

Table 1.4: The parameters of the upgrade for the FX operation

	Present	Future
Beam power	515 kW	1.3 MW
Cycle time	2.48 sec	$\leq$ 1.32 sec
Beam intensity	2.66×10^{14} ppp	$\sim 3.3 \times 10^{14}$ ppp
Capacity of the collimators	2 kW	3.5 kW

MR aims at 1.3-MW operation in the neutrino user operation, and at 100-kW operation in the hadron user operation[17, 18]. To achieve the 1.3-MW operation, MR plans to shorten the repetition rate. MR is going to upgrade the power supplies for the faster cycling time in JFY 2021. After the long shutdown the cycling time will be 1.32 sec. Besides, further studies are ongoing to realize 1.16 sec. The faster the cycling time becomes, the larger the beam loss will be. The capacity of the collimators is going to be upgraded from 2 kW to 3.5 kW. MR also plans to increase the beam intensity about 30%. To keep the present radiation dose in the ring, it is required to reduce the beam loss. The major parameters for the upgrade are listed in Table 1.4.

From the left picture of Fig. 1.6, most of the beam losses occurred in the first 0.3 sec, which corresponds to the beam energy below 6 GeV in FX operation. This was because the space charge effects were strong at the low-energy region. The space charge affects the motions of the particles through

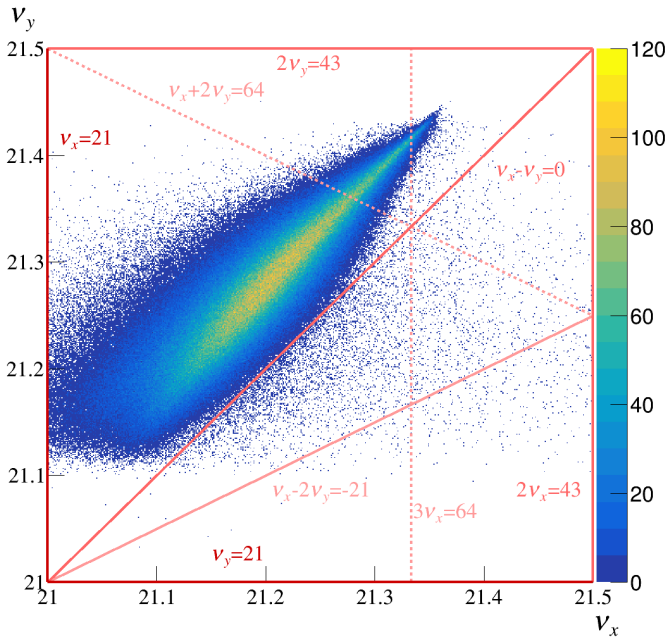

Figure 1.8: The tune spread distribution at the beam injection by SCTR and the major resonances in the neutrino user operation[21]. Each tune was calculated by the phase advance in one turn.

various mechanisms, causing the beam loss.

The operation tune in the neutrino user operation is set to $(\nu_x, \nu_y) = (21.35, 21.43)$. Actually, the tunes of all particles are not the same. The tunes are shifted particle by particle and have a certain distribution, which is called the tune spread. The tune spread is derived from the space charge effects and the momentum spread. In MR, the main cause is the former. Some particles will be on resonances due to the tune shifts. The particles will be lost if their actions exceed the physical aperture due to the effects of the resonances. Since the tune spread distribution is large in the low-energy region, the beams are affected by various kinds of the resonances, resulting in the beam loss. Therefore, it is essential to comprehend the tune spread distribution and the strengths of the resonances.

The tune spread distribution is obtained by simulations including the space charge effects. In this dissertation, simulations were performed by using SCTR (Space Charge TRacker)[42]. SCTR is a tracking code using a particle-in-cell algorithm. The details of SCTR are written in Appendix B. Figure 1.8 shows the simulation result of the tune spread distribution by SCTR and the major resonances. The tune spread distribution crosses various kinds of resonances.

The strongest resonances near the tune in FX operation are the integer resonances $\nu_x = 21$ and $\nu_y = 21$. They are excited by many kinds of sources. We will describe in Chapter 2 that the main source of them was specified as the space charge effect. There are three normal-sextupole-like resonances in Fig. 1.8: $\nu_x - 2\nu_y = -21$, $3\nu_x = 64$, and $\nu_x + 2\nu_y = 64$. Since MR has three-fold symmetry, the resonance $\nu_x - 2\nu_y = -21$ is the structure resonance. A new method to compensate it was developed and verified in Chapter 3. The resonances $3\nu_x = 64$ and $\nu_x + 2\nu_y = 64$ are the third-order nonstructure resonances. Though they are weak compared to the structure resonances $\nu_x - 2\nu_y = -21$, they have significant effects on the beam because they are close to the operation tune. These two nonstructure resonances are compensated by using the trim coils at the sextupole magnets. The details are written in Appendix C. Apert from the drawn resonances in Fig. 1.8, there are a large number of higher-order resonances. The higher-order resonances induced by the space charge effects are discussed in Chapter 4.

Chapter 2

Space Charge Effect on Integer Resonances

2.1 Sources of Integer Resonances

Integer resonances are driven by several kinds of resonant sources. The imperfection of the magnet is one of the sources. The magnet imperfection is an issue for all circular accelerators. In the accelerator employing sextupole magnets, they can induce third-order resonances. The third-order resonances can be classified into structure resonances and nonstructure resonances. Structure resonances are excited even if there are no errors. They are much stronger than nonstructure resonances. In the high-intensity accelerator, the resonances derived from the space charge effect are not negligible. They can be also classified into structure resonances and nonstructure resonances.

Let us consider the resonances in J-PARC MR, which has a three-fold symmetric structure. The operation tune is set to $(\nu_x, \nu_y) = (21.35, 21.43)$ in the present neutrino user operation. The nearest integer resonance is $\nu_x = 21$. The sextupole magnets can excite the resonance as $3\nu_x = 63$. This is a structure resonance. The space charge also excites $\nu_x = 21$. Though it causes many kinds of orders of resonances, the main effects are the second- and fourth-order resonances. In other words, the space charge excites the resonance as $2\nu_x = 42$ and $4\nu_x = 84$. These are also structure resonances.

The simple way for avoiding the effect of the space charge on the integer resonance is to change the operation tune to $(\nu_x, \nu_y) = (22.*, 22.*)$. Up to fourth order, the space charge induces resonance at $\nu_x = 22$ as $2\nu_x = 44$ and $4\nu_x = 88$. They are nonstructure resonances. The space charge effect at $\nu_x = 22$ is much weaker than at $\nu_x = 21$. It is considered that the other resonant sources have almost the same effects on $\nu_x = 21$ and on $\nu_x = 22$. In fact, the sextupole magnets excite $\nu_x = 22$ as $3\nu_x = 66$, which is also a structure resonance.

2.2 Specifying the Main Source of the Integer Resonance in J-PARC MR

2.2.1 Motivations

Operating in the region $(\nu_x, \nu_y) = (22.*, 22.*)$ is better than in the region $(\nu_x, \nu_y) = (21.*, 21.*)$ in terms of the space charge. However, it was not certain that it improves the beam operation, because the main source of the integer resonance was not clear. If the effects of magnet imperfections or the effects of sextupole magnets are much stronger than the space charge effects, the strength of the resonance $\nu_x = 21$ will be almost the same as that of the resonance $\nu_x = 22$. Conversely, if the significant difference between the two resonances is observed, it means that the main source of the resonance $\nu_x = 21$ is the space charge effect.

2.2.2 Methods

Transverse Emittance Growth

To reveal that the space charge effect is the main source of $\nu_x = 21$ or not, we measured and simulated the transverse emittance growth[21]. We set the tunes near the integer resonances, and compared the turn-by-turn horizontal emittance growths. In addition to the resonances $\nu_x = 21$ and $\nu_x = 22$, the vertical integer resonance $\nu_y = 21$ was also investigated. For simplicity, we refer to the measurements focusing $\nu_x = 21$ as the NX21 experiment, $\nu_y = 21$ as the NY21 experiment, and $\nu_x = 22$ as the NX22 experiment. Figure 2.1 shows the operation tunes and the images of the tune spread. For the NX21 experiment, some operation tunes were chosen in the range of (ν_x, ν_y) = (21.25 - 21.08, 21.43). Similarly, for the NY21 experiment, the operation tunes were chosen in the range of (ν_x, ν_y) = (21.43, 21.21 - 21.07) and in the range of (ν_x, ν_y) = (22.25 - 22.05, 22.43) for the NX22 experiment. Notable beam loss was not observed in these experiments by the DCCT[33, 34, 35, 36].

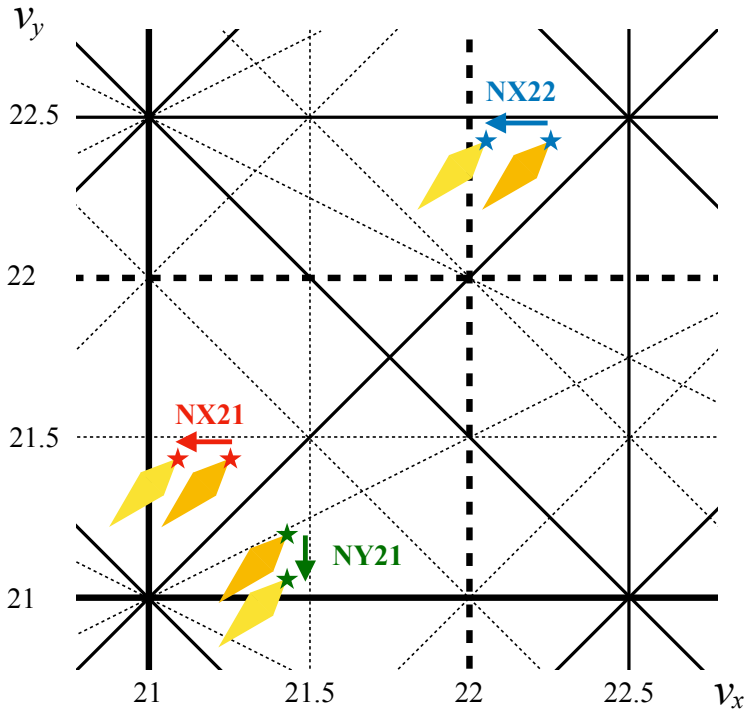

Figure 2.1: The operation tunes set in the experiments (shown as stars)[21]. The yellow diamond shapes show tune spread and the major resonance lines have been drawn. Several operation tunes were chosen in the range of (ν_x, ν_y) = (21.25 - 21.08, 21.43) for the NX21 experiment, (21.43, 21.21 - 21.07) for the NY21 experiment, and (22.25 - 22.05, 22.43) for the NX22 experiment. The space-charge-induced structure resonances have been plotted as the solid lines, while other major resonances as the dotted lines.

The initial tune spread distribution has little dependency on the tune. Even if the tune is modified, the shape of the tune spread distribution is almost kept. If the tune approaches the integer resonance, the number of particles crossing this line will increase, and the emittance grows faster. By obtaining the tune dependence of the emittance growth, the strengths of the resonances can be compared to each other. It is expected that the horizontal emittance will grow in the NX21 experiment and the NX22 experiment, and the vertical emittance will grow in the NY21 experiment. If the emittance growth of the NX21 experiment is larger than that of the NX22 experiment, it will show that the resonance $\nu_x = 21$ is stronger than $\nu_x = 22$. It is the difference between the space-charge-induced structure and nonstructure resonances.

The conditions of the beam during these experiments are shown in Table 2.1. Since the beam intensities in these experiments are relatively weak, the coherent tune shift caused by the indirect space charge effect is negligible[44].

Table 2.1: Conditions of the measurements. The beam intensities were measured by the DCCTs. The natural chromaticity is $(\xi_x, \xi_y) = (-28, -29)$.

		NX21	NY21	NX22
Intensity		5.3×10^{12} ppb	3.3×10^{12} ppb	3.3×10^{12} ppb
Tune (ν_x, ν_y)		(21.*, 21.43)	(21.43, 21.*)	(22.*, 22.43)
Maximum tune shift	$\lvert\Delta\nu_{x,\max}\rvert$	0.35	0.30	0.30
	$\lvert\Delta\nu_{y,\max}\rvert$	0.36	0.33	0.33
Chromaticity (ξ_x, ξ_y)			$(-7, -7)$	

The experiments were conducted using single bunch beams. We observed the developments of the horizontal profiles in the first 100 turns after the injection. The turn-by-turn beam positions and sizes were calculated by fitting the integrated signals. We use the fitting function as follows:

$$f(x) = A\left(1 - \frac{1}{n}\frac{(x - x_0)^2}{w^2}\right)^n + C. \tag{2.1}$$

This function is identical to a Gaussian for $n \to \infty$ and to a parabola at $n = 1$. The half width at half maximum (HWHM) was taken as the beam size. The tunes were obtained by a discrete Fourier transform of 100 turns of the center positions x_0. Therefore, the resolution of the tune is estimated within 0.01.

Though the injected beam is Gaussian, the beam tail grew and the beam profile became distorted when the tune was close to the integer resonance. However it had little effects on our results because we focused on the discussion about the beam core by defining the beam width as the HWHM. The cores of the profiles were fitted with good precision by the fitting function given by Eq. (2.1).

Profile Monitor

In the measurements, the turn-by-turn horizontal beam sizes were obtained by the Multi-Ribbon Profile Monitor (MRPM)[45, 46, 47]. In the main ring, a MRPM is situated at the beam injection position. It is called Inj-MRPM. It can measure turn-by-turn beam profiles up to about 100 turns. It is located in the dispersion-free area. Inj-MRPM is made of five layers, in order, solid graphite electrode, graphite ribbons, solid titanium electrode, titanium ribbons, and solid graphite electrode. [†] In this study, 11 ribbons were used in total to measure the horizontal beam profiles. Inj-MRPM obtains beam profiles by measuring the current of secondary electrons, which are emitted from its surface when the beam passes. The signals of Inj-MRPM were integrated for each channel and each turn to reconstruct the turn-by-turn beam profiles.

Since the beam hits Inj-MRPM many times, the beam size grows by the multiple scattering. The scattering angles of the particles follow a Gaussian distribution[48]. As the transverse beam profile is Gaussian at the beam injection in MR, the scattered beam profile is also Gaussian. By convolution calculations, the scattered beam size σ_n after n turns becomes

$$\sigma_n^2 = \sigma_{\text{init}}^2 + n\sigma_{\text{scat}}^2, \tag{2.2}$$

where σ_{init} is the initial beam size and σ_{scat} represents the growth term in one turn due to the multiple scattering. The effect of the multiple scattering does not depend on the tune. The scattering angle can be estimated from the data in which the tune is far enough from the resonances.

[†]The order of five layers was changed after these experiments.

The specification of Inj-MRPM is listed in Table 2.2.

Table 2.2: Inj-MRPM specifications[21]. The thickness of the electrodes is the same as the ribbons.

	Horizontal	Vertical
Material	Graphite	Titanium
Ribbon pitch	4.5 mm	2.5 mm
Ribbon width	3.0 mm	1.5 mm
Thickness	3 μm	1 μm

Other Contributions to the Emittance Growth

In addition to the multiple scattering, there are some systematic errors for the measurements.

One is the beam dilution occurring due to the beta mismatch at the injection. The beam size fluctuates during the first several turns and its oscillation is damped due to the space charge effect. The amplitude of the oscillation can depend on the tunes because the Twiss parameters at the injection depend on the tunes. To suppress the oscillation, we adjusted the optics of the transport line at each tune.

Another contribution to the emittance growth is the effect of the sextupoles. Since both the resonances $\nu_x = 21$ and $\nu_x = 22$ are the sextupole-driven structure resonances, the sextupole magnetic fields can induce them. Evaluations of these effects are provided in section 2.3.

Other than the above-mentioned sextupole effect, the beam encounters unexpected quadrupole magnetic fields if there are offsets between the beam position and the center of the sextupole magnets. Misalignments of the sextupole magnets and closed orbit errors produce DC offsets and can cause tune shifts and strengthening of resonances. The dipole oscillation at the sextupole magnets produces AC offsets. It causes the oscillation of the beam size with the frequency of the dipole oscillation. The amplitude of the oscillation of the quadrupole magnetic field produced by the sextupole magnets depends not only on the AC offset, but also on the DC offset. The oscillation of the quadrupole magnetic field is larger when the DC offset is larger. In the experiments, the closed orbit was corrected at $(\nu_x, \nu_y) = (21.35, 21.43)$ and $(22.30, 22.40)$. The correction was not repeated during the tune scan. The closed orbit errors were larger when the tune was closer to the integer resonance. The betatron oscillation amplitude at the beam injection was corrected within 1 mm.

Simulation Approach

The basic optics was obtained by using the strategic accelerator design (SAD)[49] program. The tracking simulations were performed using the space charge tracker (SCTR)[42] program. SCTR is a simulation code including the space charge effect using a particle-in-cell algorithm. The detailed explanations for SCTR are written in Appendix B. The number of macro particles in this simulation was 200,000. The conditions of the simulations are the same as those of experiments. The details are listed in Table 2.3. As error sources, the alignment errors and magnetic field gradient errors were considered[50].

The initial transverse emittance was determined by the data whose tunes were far from the integer resonance. Figure 2.2 shows turn-by-turn beam sizes. The tunes were set to $(\nu_x, \nu_y) = (21.25, 21.43)$. The fluctuation of the beam size during the first 10 turns was caused by the beta mismatch at the injection. It damped within 10 turns due to the dilution. In order to evaluate the emittance at the injection and the scattering angle, the plots from turn 11 to turn 100 were fitted to a linear function Eq. (2.2). The initial emittance was calculated using σ_{init} of the function Eq. (2.2). Since Inj-MRPM is located in a dispersion-free area, we calculated the emittances using $\varepsilon = \sigma_{\mathrm{init}}^2/\beta$. In this condition, the betatron function at Inj-MRPM was 16.3 m, which was obtained by SAD. The initial phase-space beam distribution was slightly modified from the matching condition to reproduce the effect of the residual beta mismatch

Table 2.3: Initial conditions of the simulations.

	NX21	NY21	NX22
Intensity	5.3×10^{12} ppb	3.3×10^{12} ppb	3.3×10^{12} ppb
Tune (ν_x, ν_y)	(21.*, 21.43)	(21.43, 21.*)	(22.*, 22.43)
Transverse distribution		Gaussian	
Transverse emittance $\varepsilon_x, \varepsilon_y$	1.1π mm mrad	0.85π mm mrad	0.85π mm mrad
Longitudinal distribution		Parabola	
Longitudinal beam size	52 ± 1 m	46 ± 2 m	46 ± 2 m
Momentum spread $\Delta p/p$		0.004	
Chromaticity (ξ_x, ξ_y)		$(-7, -7)$	

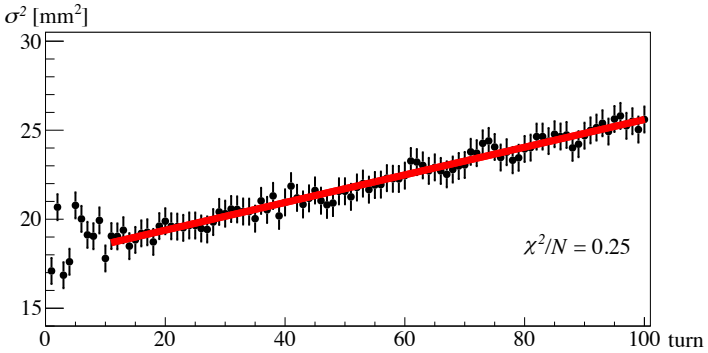

Figure 2.2: The turn-by-turn beam sizes[21]. The error bars show statistical errors. The red line represents the linear fitting to the plots.

at the injection. The dipole errors at the beam injections were not applied in the simulations. The same procedure was carried out for the NY21 and NX22 experiments.

The longitudinal beam profiles were measured by the wall current monitor (WCM)[51]. The initial longitudinal distribution was parabolic. For the estimation of the longitudinal beam size, we define the bunching factor B_f as the ratio of the average amplitude to the peak amplitude of the signals of the wall current monitor. We set the bunching factor $B_f \sim 0.2$. The momentum spreads were adjusted so that the longitudinal beam profiles at the 100 turns of the simulations were the same as those in the experiments.

The multiple scattering at Inj-MRPM was also implemented in the simulations. Each particle is scattered turn by turn with a random angle following a Gaussian distribution. We set the rms of the scattering angles as $\theta_{x,\mathrm{rms}} = 24$ μrad. It was determined such that the simulation demonstrated the emittance growth of the experiments shown in Fig. 2.2. The scattering angle can also be calculated as[48]

$$\theta_{x,\mathrm{rms}} = \frac{13.6\ \mathrm{MeV}}{\beta_{\mathrm{rel}} cp} z \sqrt{\frac{x}{X_0}} \left[1 + 0.038 \log \left(\frac{xz^2}{X_0 \beta_{\mathrm{rel}}^2} \right) \right], \tag{2.3}$$

where $\beta_{\mathrm{rel}}c, p$, and z are the velocity, momentum, and charge number of the beam particle respectively, x is the thickness of the target, and X_0 is the radiation length of the target. Using this expression, the rms of the scattering angle at each layer was calculated. The thicknesses of targets are given in Table 2.2 and the radiation lengths are 42.70 g/cm^2 (Graphite) and 16.17 g/cm^2 (Titanium)[52]. The total scattering angle, derived by square root of the sum of squares of each angle, was $\theta_{x,\mathrm{rms}} = 20$ μrad and is consistent with the simulation results.

2.2.3 Result

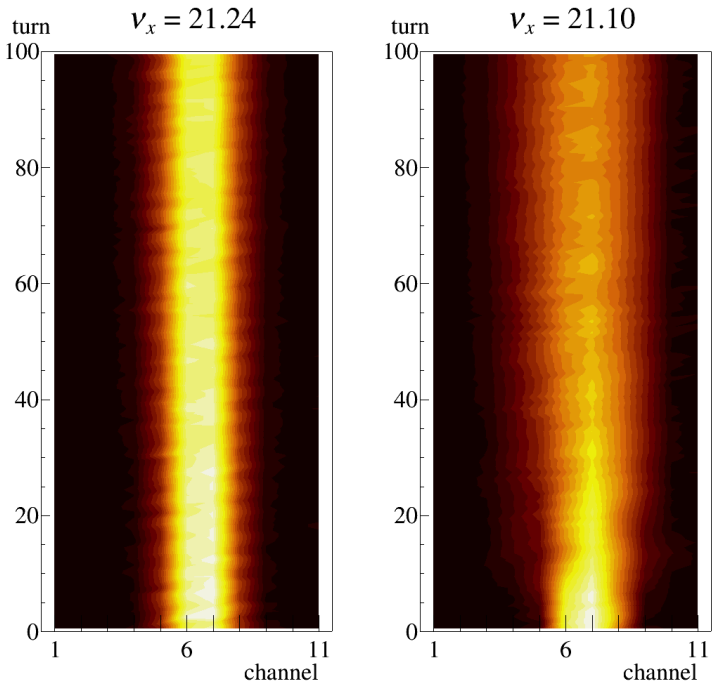

Figure 2.3: Turn-by-turn integrated signals of Inj-MRPM in the horizontal plane[21]. The figure on the left shows the result under the condition of (ν_x, ν_y) = (21.24, 21.43), and the one on the right shows the result under the condition of (ν_x, ν_y) = (21.10, 21.43). The horizontal axes represent the ribbon channels and the vertical axes represent the turns. The pitch of the adjacent channels was 4.5 mm.

Figure 2.3 shows examples of the integrated signals of Inj-MRPM in the horizontal plane. The left picture is the result at the tune (ν_x, ν_y) = (21.24, 21.43). In this condition, no clear dipole or quadrupole oscillations were seen. The right picture is the result at the tune (ν_x, ν_y) = (21.10, 21.43). The emittance grew rapidly in 100 turns. There was an oscillation with a period of 10 turns after about 40 turns. This period corresponds to the frequency of the dipole oscillation at this tune. It is interpreted as the effect of the beam orbit distortions.

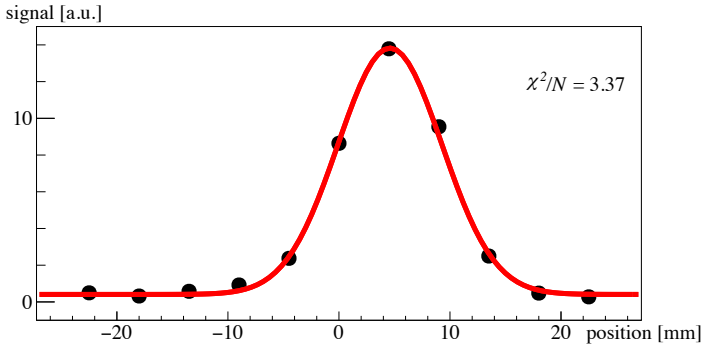

Figure 2.4: Example of integrated signals of Inj-MRPM[21]. The black points represent the integrated signals of Inj-MRPM and the red line represents the fitting. This is the data at the turn 10 of the beam and corresponds to the condition (ν_x, ν_y) = (21.08, 21.43).

Figure 2.4 shows the integrated signals of the Inj-MRPM and a corresponding fitting to the data points. When the tune was near the integer resonance, the profile was distorted from a Gaussian.

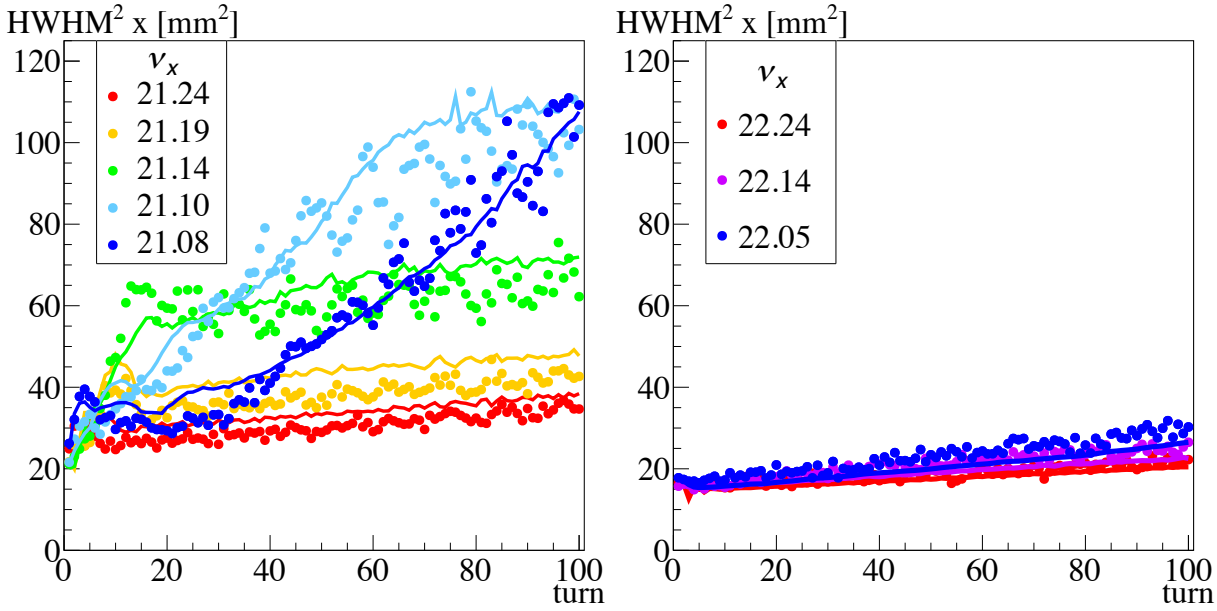

Figure 2.5: Horizontal beam sizes in the NX21 experiment (left) and in the NX22 experiment (right)[21]. Experimental results are shown as circles and simulation results are shown as lines. The color difference represents the difference in the horizontal tunes. The vertical tunes were fixed to $\nu_y = 21.43$ in the NX21 experiment, and to $\nu_y = 22.43$ in the NX22 experiment.

Figure 2.5 shows the turn-by-turn horizontal beam sizes in the NX21 experiment and the NX22 experiment respectively. In the NX21 experiment, the growth of the horizontal beam sizes strongly depended on the horizontal tune. The emittance grew by a factor of 1.5 at $\nu_x = 21.24$ in 100 turns, and by a factor of 5 at $\nu_x = 21.10$ in the experiments. In the NX22 experiment, the beam size grew almost linearly with the turns. The dependency of the growth on the horizontal tune was small. The emittance grew by a factor of 1.4 at $\nu_x = 22.24$, and by a factor of 1.8 at $\nu_x = 22.05$ in the NX22 experiment. The main reason for the emittance growth in the NX22 experiment is the multiple scattering at Inj-MRPM. Comparing the two experiments, the beam grew much slower in the NX22 experiment. Although the tune spread was smaller by a factor of 0.86 in the NX22 experiment, it cannot explain the slow growth. The measured difference between the NX21 experiment and the NX22 experiment was exactly the difference between the structure resonance and the nonstructure resonance. It clearly shows that the space charge effect is the main source for the resonance $\nu_x = 21$.

Figure 2.6 shows the turn-by-turn horizontal beam sizes in the NY21 experiment. In the NY21 experiment, the growth ratios of the horizontal beam sizes did not depend on the vertical tune. The emittance grew by a factor of 1.6 for all tunes in the experiments. Comparing the NX21 experiment to the NY21 experiment, it is clear that $\nu_x = 21$ affected only the horizontal profiles and $\nu_y = 21$ affected only the vertical profiles. The linear emittance growths are derived from the multiple scattering at the Inj-MRPM.

The simulation results were in good agreement with the experimental results in all conditions. It shows that these results were caused by the space charge effect. At the same time, the simulation code (SCTR) was well benchmarked. Though the simulations contained the effects derived from imperfections of the magnets in Fig. 2.5 and in Fig. 2.6, the results of the NX21 experiment can be reproduced only by the effect of the space charge and the multiple scattering. This fact also reinforces that the main source

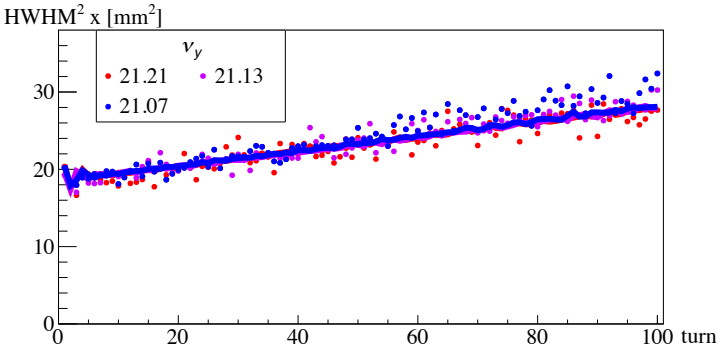

Figure 2.6: Horizontal beam sizes in the NY21 experiment[21]. Experimental results are shown as circles and simulation results are shown as lines. The color difference represents the difference in the vertical tune. The horizontal tunes were fixed to $\nu_x = 21.43$.

of the resonance $\nu_x = 21$ is the space charge effect.

Let us move to the detailed explanations of the NX21 experiment. The various growths in the NX21 experiment reflected the tune spread distribution of the beam. In the case of $\nu_x = 21.24$, the beam size grew slowly and linearly. This is because the tune was far enough from the resonance $\nu_x = 21$. The source of growth was the multiple scattering. For the case of $\nu_x = 21.14$, a fast growth was observed in the first 15 turns. This is interpreted that the core of the tune spread distribution was crossing $\nu_x = 21$ at the injection, resulting in a rapid emittance growth. After a fast growth in first turn 15, the tune spread was smaller owing to the emittance growth. The major part of the tune spread distribution shifted above the resonance $\nu_x = 21$, and the emittance growth became slow. The slow and linear growth after turn 15 is due to multiple scattering. In the case of $\nu_x = 21.08$, the beam size did not grow for the first 30 turns. This can be understood that the core of the tune spread was below $\nu_x = 21$. At the beam injection, the particles at the beam tail were on the resonances, still the particles at the beam core were out of its effect. However, the core of the tune spread gradually moved close to the integer resonance line, because the beam tail grew and the space-charge force was weakened. The core of the tune spread began crossing the integer resonance after turn 30, causing beginning a rapid emittance growth. From these considerations, the core of the tune spread distribution at the injection was thought to be around -0.14 from the operation tune.

In some cases, a small systematic difference was observed between the results of the experiments and simulations. One of the reasons is the systematic error in the background estimations of the signals of Inj-MRPM. There were only 11 channels used for the measurements, and this made it difficult to evaluate the signal background. The small beam sizes in the experiments can be explained by the background overestimation. Not only the number of channels, but also wide pitches of ribbons affected the measurements. When the beam size was small, only a few channels signaled. It could make systematic errors larger. Another possible cause of the systematic differences is that the initial beam distribution might have deviated from the Gaussian distribution. A real detailed distribution could be obtained if there were more channels.

2.3 Evaluation of the Space Charge Effect

2.3.1 Incoherent Detuning and Resonance Width

So far, the strengths of the resonances were compared. There was a clear tune dependence of the beam growth for the strong resonance. It is important to evaluate not only the strengths of resonances but also the effect on the beam. In this section, we will discuss how the particle feels the resonance.

We start the discussion by assuming the beam distribution is a Gaussian. The linear tune shift is a function of the actions J_x, J_y. From Eq. (1.61, 1.62, 1.64), it can be written as

$$\Delta\nu_u(J_x, J_y) = -\frac{\lambda r_0}{\gamma_{\rm rel}^3\beta_{\rm rel}^2}\frac{1}{2\pi}\oint \mathrm{d}s\frac{\beta_u}{(\sigma_x^2+\sigma_y^2)}\int_1^\infty \mathrm{d}\zeta\frac{e^{-w_x-w_y}[I_0(w_u)-I_1(w_u)]I_0(w_v)}{(\zeta+\Delta_{uv})^{3/2}(\zeta+\Delta_{vu})^{1/2}}, \tag{2.4}$$

where λ is the line density, r_0 is the classical radius of the particle, $\gamma_{\rm rel}, \beta_{\rm rel}$ are the Lorentz factors, β_u is the betatron function, σ_u is the rms beam size,

$$\Delta_{xy} = -\Delta_{yx} = \frac{\sigma_x^2-\sigma_y^2}{\sigma_x^2+\sigma_y^2}, \tag{2.5}$$

$$w_u = -\frac{J_u\beta_u}{(\sigma_x^2+\sigma_y^2)(\zeta+\Delta_{uv})} \qquad ((u,v)=(x,y),(y,x)), \tag{2.6}$$

and $I_\nu(z)$ is the modified Bessel function. The condition that a particle is on the resonance can be written as

$$m_x\nu_x(J_{xR}, J_{yR}) + m_y\nu_y(J_{xR}, J_{yR}) = l, \tag{2.7}$$

where

$$\nu_u(J_x, J_y) = \nu_{u0} + \Delta\nu_u(J_x, J_y), \tag{2.8}$$

ν_{u0} is the bare tune, (J_{xR}, J_{yR}) is the pair of actions satisfying the resonance condition, and m_x, m_y, l are the integers. The resonance has effects on the particles whose action is around (J_{xR}, J_{yR}). Hereinafter, let us consider the horizontal resonance, meaning $m_y = 0$. Defining the resonance width ΔJ_x as the width of the action region where the resonance affects, it can be written as from Eq. (1.53, 1.54, 1.59, A.22),

$$\Delta J_x = 4\sqrt{\frac{V_{k,0}(J_{xR})}{\Lambda}}, \tag{2.9}$$

where

$$\Lambda = \frac{\partial^2\bar{U}_{0,0}}{\partial J_x^2}(J_{xR}) \tag{2.10}$$

$$= \frac{\lambda r_0}{\gamma_{\rm rel}^3\beta_{\rm rel}^2}\frac{1}{2\pi}\oint \mathrm{d}s\frac{\beta_x^2}{(\sigma_x^2+\sigma_y^2)^2}\int_0^1 \mathrm{d}\tau\ \frac{e^{-w_x-w_y}[\frac{3}{2}I_0(w_x)-2I_1(w_x)+\frac{1}{2}I_2(w_x)]I_0(w_y)}{(1+\Delta_{xy}\tau)^{5/2}(1-\Delta_{xy}\tau)^{1/2}}\Bigg|_{J_{xR}}, \tag{2.11}$$

$$\bar{U}_{0,0} = \frac{\lambda r_0}{\gamma_{\rm rel}^3\beta_{\rm rel}^2}\frac{1}{2\pi}\oint \mathrm{d}s\int_1^\infty \mathrm{d}\zeta\frac{e^{-w_x-w_y}I_0(w_x)I_0(w_y)}{\sqrt{\zeta^2-\Delta_{xy}^2}}, \tag{2.12}$$

and $V_{k,0}$ is the potential of the k th resonance. The space charge excites multi-order resonances. Especially the second- and fourth-order resonances are strong. Their potentials are from Eq. (1.59)

$$V_{2,0} = 2\left|\frac{\lambda r_0}{\gamma_{\rm rel}^3\beta_{\rm rel}^2}\frac{1}{2\pi}\oint \mathrm{d}s e^{i2\psi_x}\int_1^\infty \mathrm{d}\zeta\frac{e^{-w_x-w_y}I_1(w_x)I_0(w_y)}{\sqrt{\zeta^2-\Delta_{xy}^2}}\right|, \tag{2.13}$$

$$V_{4,0} = 2\left|\frac{\lambda r_0}{\gamma_{\rm rel}^3\beta_{\rm rel}^2}\frac{1}{2\pi}\oint \mathrm{d}s e^{i4\psi_x}\int_1^\infty \mathrm{d}\zeta\frac{e^{-w_x-w_y}I_2(w_x)I_0(w_y)}{\sqrt{\zeta^2-\Delta_{xy}^2}}\right|, \tag{2.14}$$

where ψ_x is the horizontal phase advance. Sextupole magnets induce the third-order resonance. Its potential is [53]

$$V_{3,0} = 2\left|\frac{\sqrt{2}}{24\pi}J_x^{3/2}\oint \mathrm{d}s\beta_x^{3/2}K_2 e^{i3\psi_x}\right|, \tag{2.15}$$

where K_2 is the strength of the sextupole magnetic field. Hereinafter, the resonance widths derived from $V_{2,0}, V_{4,0}, V_{3,0}$ are written $\Delta J_{\mathrm{spch},2}, \Delta J_{\mathrm{spch},4}, \Delta J_{\mathrm{sext}}$, individually.

To evaluate the resonant effect at NX21 experiment and at the NX22 experiment in the previous section, we calculated the incoherent tune shifts and the resonance widths. In the calculations of the potentials, we use the modified horizontal phase advance by the space charge effect. The results are shown in Table 2.4.

Table 2.4: The action of the on-resonance particle $2J_{xR}$ and the resonance widths $2\Delta J$ calculated analytically.

Bare tune ν_{x0}	$2J_{xR}$ [μm]	$2\Delta J_{\mathrm{spch},2}$ [μm]	$2\Delta J_{\mathrm{spch},4}$ [μm]	$2\Delta J_{\mathrm{sext}}$ [μm]
21.08	9.3	16.3	11.6	6.0
21.14	4.2	4.4	4.4	2.7
21.24	1.4	2.9	1.4	1.0
22.05	12.2	0	0	6.9
22.14	3.0	0	0	1.5
22.24	0.7	0	0	0.4

2.3.2 Visualization of Resonances on the Poincaré Map

The actions of the on-resonance particles J_{xR} and the resonance widths ΔJ in the NX21, NX22 experiments were also simulated by SCTR. In order to evaluate the effect of the space-charge-induced resonance on particles, “frozen model" simulations were performed. The frozen model fixes all the space charge potentials to the values at a certain turn. In this study, we fixed potentials at the first superperiod of the first turn. Since the space charge forces are fixed, the beam feels the same multipole fields at every turn. As a result, space-charge-induced resonances appear clearly. We excluded the effects of the multiple scattering and magnet imperfections in order to make the discussion simpler.

We drew the Poincaré maps for the conditions of the NX21 experiment and the NX22 experiment. If a particle is far enough from the resonance, it traces a round trajectory in the normalized phase-space coordinates. Converting them into the action-angle coordinates, the action is constant. On the other hand, if it is captured by some resonance, its trajectory will be an island. Generally, the nth-order resonance makes n resonance islands.

Figure 2.7 shows the Poincaré maps with the condition of the bare tune ν_{x0} = 21.24, 21.14, and 21.08 using the frozen model. The figures in the top row are drawn with the normalized phase-space coordinates $x - p_x$, and those in the bottom row are drawn with the action-angle coordinates $\psi_x - J_x$. The incoherent tunes of the particles drawn in Fig. 2.7 are shown in Fig. 2.8.

From the Poincaré maps of ν_{x0} = 21.24, no clear resonance island was observed. This explains the small emittance growth at ν_{x0} = 21.24. From the Poincaré maps of ν_{x0} = 21.14, the particles whose actions were $2J_x \lesssim 7$ μm were affected by the resonance. From its shape, it is revealed that the second-order resonance was the main source. From Fig. 2.8, it is confirmed that the incoherent tunes of the particles on the resonance (shown by orange and red colors) are almost 21. Considering that the emittance of the beam was set to 1.1π mm mrad, most of the particles were under the influence of the space-charge-induced structure resonance.

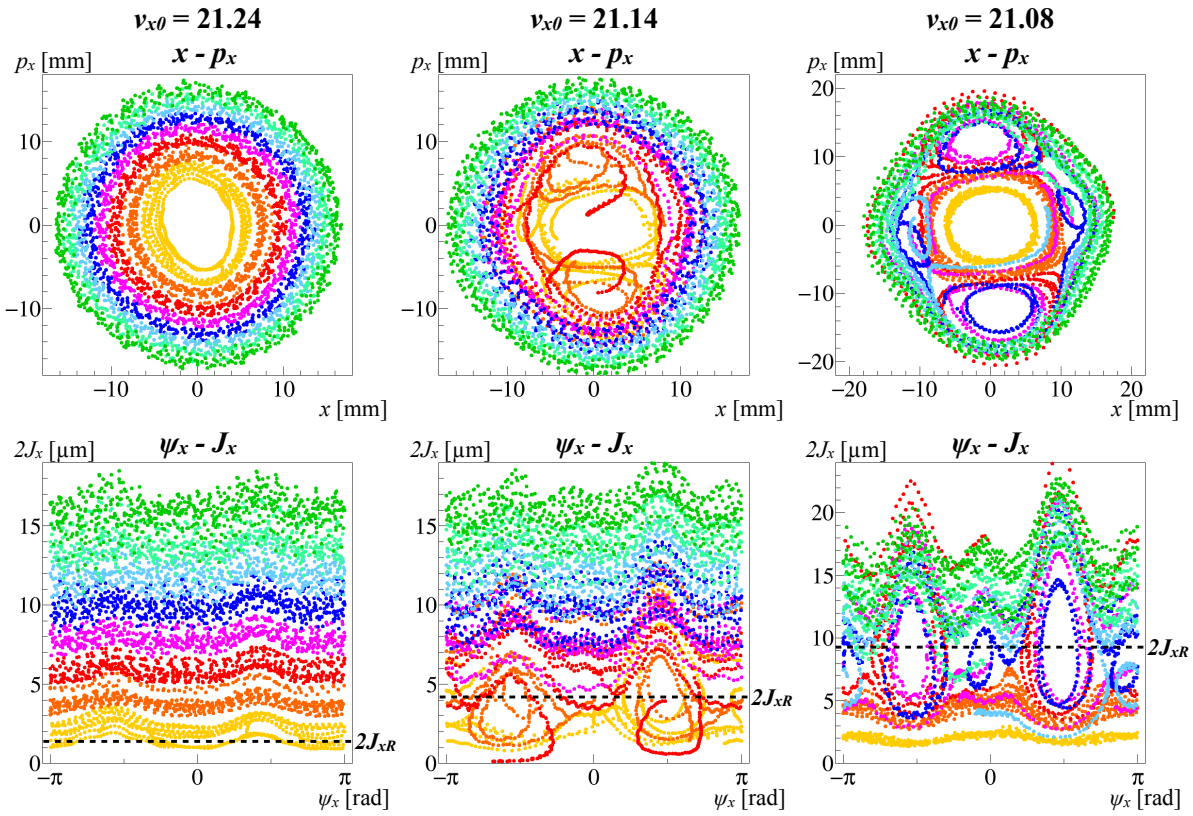

Figure 2.7: Poincaré maps obtained from SCTR simulations using the frozen model[21]. The left panel corresponds to ν_{x0} = 21.24, the center panel to ν_{x0} = 21.14, and the right panel to ν_{x0} = 21.08. The top row shows the Poincaré maps of the normalized phase-space coordinates and the bottom row shows those of the action-angle coordinates. The same colors represent the same action in all plots. The black dotted lines in the bottom row figures show the on-resonance actions by the analytical calculations listed at Table 2.4.

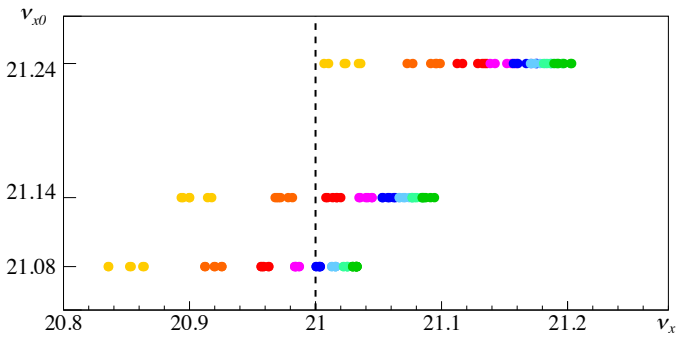

Figure 2.8: Incoherent tunes in the NX21 experiment obtained by simulations[21]. The vertical axis represents the bare tune and the horizontal axis represents the incoherent tune. Different actions have been plotted with different colors. The color codes are the same as in Fig. 2.7.

The Poincaré maps corresponding to ν_{x0} = 21.08 indicate not only the effect of a second-order resonance but also that of a fourth-order resonance. Both the second- and fourth-order resonances are due to the space charge effect. The particles whose actions were $2J_x \lesssim 4$ μm were out of the resonance. As can be seen from Fig. 2.8, the incoherent tune of the orange particles ($2J_x \sim 4$ μm) is about 0.08

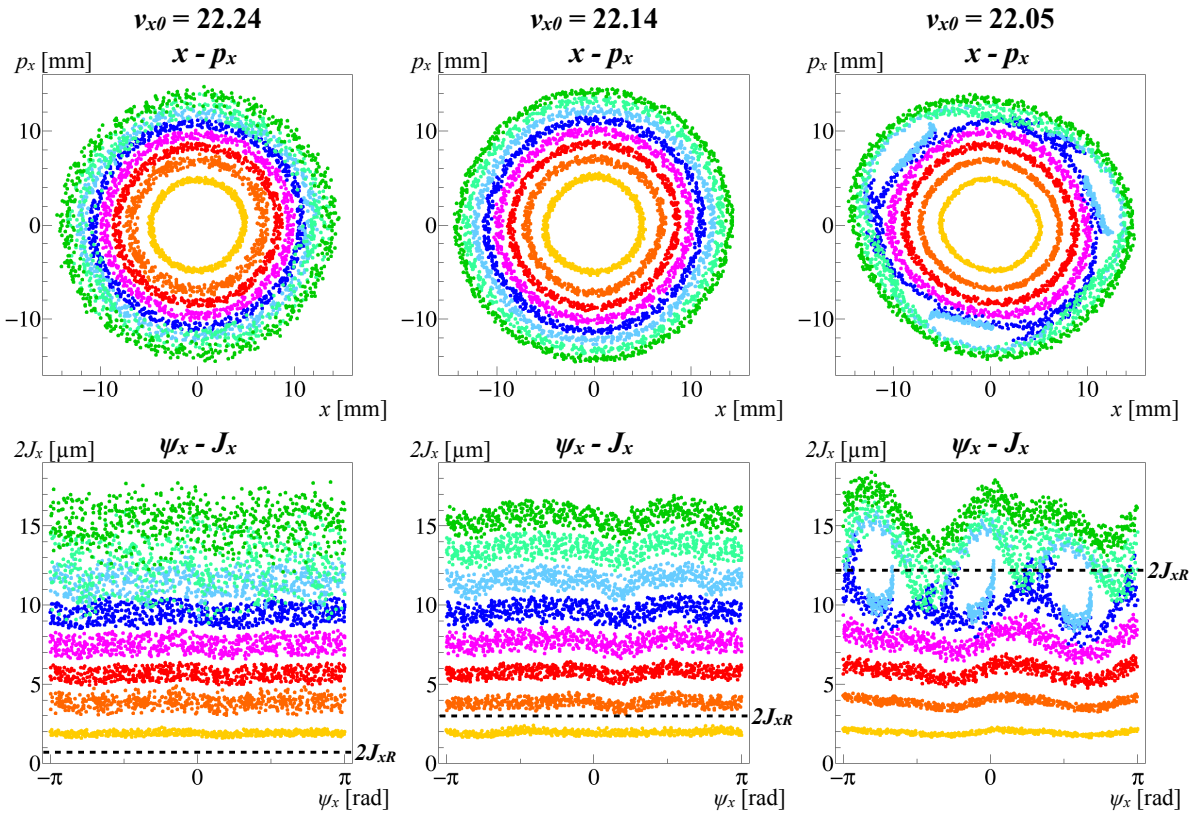

Figure 2.9: Poincaré maps obtained from SCTR simulations using the frozen model[21]. The left panel corresponds to ν_{x0} = 22.24, the center panel to ν_{x0} = 22.14, and the right panel to ν_{x0} = 22.05. The top row shows the Poincaré maps of the normalized phase-space coordinates and the bottom row shows those of the action-angle coordinates. The same colors represent the same action in all plots. The black dotted lines in the bottom row figures show the on-resonance actions by the analytical calculations listed at Table 2.4.

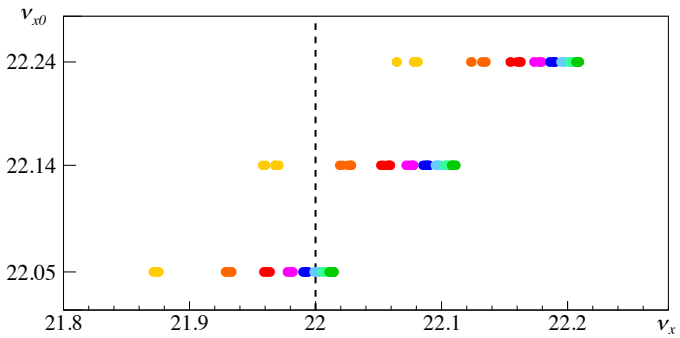

Figure 2.10: Incoherent tunes in the NX22 experiment obtained by simulations[21]. The vertical axis represents the bare tune and the horizontal axis represents the incoherent tune. Different actions have been plotted with different colors. The colors are the same as in Fig. 2.9.

away from ν_x = 21, and that of the yellow particles ($2J_x \sim 2$ μm) is about 0.15 away from ν_x = 21. This indicates that the particles around the beam core were out of the range of the space-charge-induced resonance and explains the stable beam size for the first 30 turns.

The actions of the on-resonance particles $2J_{xR}$ by the analytical calculation listed in Table 2.4 have

also been plotted in Fig. 2.7 as black dotted lines. In all conditions, the analytical $2J_{xR}$ lines are at the center of the resonance islands obtained by the simulations. The analytical resonance widths indicate that the space-charge-induced resonances are stronger than the sextupole-induced resonance in the NX21 experiment. It was also reflected in the simulations.

Figure 2.9 shows the Poincaré maps of ν_{x0} = 22.24, 22.14, and 22.05 obtained by the frozen model simulations. The incoherent tunes in these conditions are shown in Fig. 2.10. In the case of the Poincaré maps of ν_{x0} = 22.24, the beam was not affected by resonances. In fact, the incoherent tunes of the tracking particle were far from 22, as can be seen from Fig. 2.10. In the Poincaré maps of ν_{x0} = 22.14, resonance islands were not observed clearly. Large third-order resonance islands could be seen for the case of ν_{x0} = 22.05. The incoherent tunes of the on-resonance particles were around $\nu_x = 22$ as is observed from Fig. 2.10. Since the space charge does not induce odd-order resonances, the integer resonance $\nu_x = 22$ was excited by the sextupole magnetic fields.

The mechanism of the excitation of the integer resonance by the sextupole magnetic fields is complicated. In J-PARC MR, the main sources of the sextupole magnetic fields are the sextupole magnets and the high-order fields by the bending magnets. Both the sextupole magnets and the bending magnets are located in the arc sections. One arc section is made of eight symmetric modules. Since the horizontal phase advance of the one module is set to $\Delta\psi_{\mathrm{mod},x} = 0.75\pi$ rad, the resonance driving terms $G_{3,0,63}, G_{3,0,66}$ are basically canceled (detailed explanations are described in Chapter 3). The resonances $\nu_x = 21$ and $\nu_x = 22$ are not excited by the sextupole magnetic fields in the bare optics, if there are no magnet imperfections. However, due to the space charge effects, the phase advance is shifted. The cancelation is broken, and the resonances $\nu_x = 21$ and $\nu_x = 22$ are excited by the sextupole magnetic fields even if there are no errors. This is the reason why the resonance widths were calculated with the shifted phase advances in Table 2.4. If the bare phase advances are used, ΔJ_{sext} will be zero in all conditions. These calculations were supported by the simulation result at $\nu_{x0} = 22.05$, which clearly indicated the existence of the sextupole-driven resonance.

The black dotted lines in Fig. 2.9 show $2J_{xR}$ listed in Table 2.4. The analytical $2J_{xR}$ line of ν_{x0} = 22.05 is at the center of the resonance islands obtained by the simulations. The analytical resonance width was also consistent with the resonance width shown by simulation.

In any tune at $\nu_{x0} = 22.*$, second- or fourth-order resonance islands did not appear. This is consistent with the fact that $\nu_x = 22$ is a nonstructure resonance for the space charge. Strictly, considering higher-order, $\nu_x = 22$ is a sixth-order space-charge-driven structure resonance. However, Fig. 2.9 shows that the sixth-order resonance is negligible in this intensity. The integer resonance $\nu_x = 22$ is not excited by the space charge effect unless there are optics errors.

Chapter 3

Compensation of Third-Order Structure Resonances

本章については、５年以内に雑誌等で刊行予定のため、非公開。

Chapter 4

Compensation of the Space-Charge-Induced Resonances

本章については、５年以内に雑誌等で刊行予定のため、非公開。

Chapter 5

Conclusions

本章については、５年以内に雑誌等で刊行予定のため、非公開。

Appendix A

Calculation of Space Charge Potential

The space charge potential of the two-dimensional Gaussian beam is[24]

$$U(x,y;s) = \frac{\lambda r_0}{\gamma_{\rm rel}^3\beta_{\rm rel}^2}\int_0^\infty \mathrm{d}q \frac{\exp(-\frac{x^2}{2\sigma_x^2+q}-\frac{y^2}{2\sigma_y^2+q})}{\sqrt{2\sigma_x^2+q}\sqrt{2\sigma_y^2+q}}, \tag{A.1}$$

where λ is the line density, r_0 is the classical radius of the particle, $\gamma_{\rm rel}, \beta_{\rm rel}$ are the Lorentz factors, and σ_u is the rms beam size. Changing the coordinates from (u,u') to (ψ_u, J_u) by using

$$u = \sqrt{2J_u\beta_u}\cos\psi_u, \qquad \psi_u = \int \frac{\mathrm{d}s}{\beta_u} \tag{A.2}$$

the space charge potential becomes

$$U(\psi_x,\psi_y,J_x,J_y;s) = \frac{\lambda r_0}{\gamma_{\rm rel}^3\beta_{\rm rel}^2}\int_0^\infty \mathrm{d}q \prod_{u=x,y}\frac{\exp[-w_u(1+\cos 2\psi_u)]}{\sqrt{2\sigma_u^2+q}}, \tag{A.3}$$

where

$$w_u = \frac{J_u\beta_u}{2\sigma_u^2+q}. \tag{A.4}$$

Changing the independent variable from the path length s to the orbiting angle $\theta \equiv 2\pi s/C$, where C is the circumference, and the coordinates from (ψ_u, J_u) to $(\phi_u, \bar{J}_u)$ by using

$$\phi_u = \psi_u - \chi_u + \nu_u\theta, \qquad \chi_u(s) = \int_{s_0}^{s}\frac{\mathrm{d}s}{\beta_u}, \tag{A.5}$$

the space charge potential can be written as

$$U(\phi_x,\phi_y,J_x,J_y;\theta) = \frac{C}{2\pi}\frac{\lambda r_0}{\gamma_{\rm rel}^3\beta_{\rm rel}^2}\int_0^\infty \mathrm{d}q \prod_{u=x,y}\frac{\exp[-w_u(1+\cos\{2\phi_u+2\chi_u-2\nu_u\theta\})]}{\sqrt{2\sigma_u^2+q}}. \tag{A.6}$$

Writing the potential as Fourier series of ϕ_x, ϕ_y, it becomes

$$U(\phi_x,\phi_y,J_x,J_y;\theta) = \sum_{m_x,m_y}\tilde{U}_{m_x,m_y}(J_x,J_y;\theta)e^{i[m_x\phi_x+m_y\phi_y]}, \tag{A.7}$$

$$\tilde{U}_{m_x,m_y}(J_x,J_y;\theta) = \frac{1}{(2\pi)^2}\iint U(\phi_x,\phi_y,J_x,J_y;\theta)e^{-i[m_x\phi_x+m_y\phi_y]}\mathrm{d}\phi_x\mathrm{d}\phi_y. \tag{A.8}$$

Using

$$\begin{aligned}
&\frac{1}{2\pi}\int_0^{2\pi} \mathrm{d}\phi \exp[-w(1+\cos(2\phi+2\xi)) - im\phi] \\
&= \frac{1}{4\pi}\int_0^{4\pi} \mathrm{d}\varphi \exp[-w(1+\cos\varphi) - im(\varphi/2-\xi)] \\
&= \frac{1}{4\pi} e^{-w+im\xi}\left[\int_0^{2\pi} \mathrm{d}\varphi e^{-w\cos\varphi - im\varphi/2} + \int_0^{2\pi} \mathrm{d}\varphi e^{-w\cos\varphi - im\varphi/2 - im\pi}\right] \\
&= \frac{1}{2\pi} e^{-w+im\xi}\int_0^{2\pi} \mathrm{d}\varphi e^{-w\cos\varphi - im\varphi/2} \qquad (m = \text{even}) \\
&= -e^{-w+im\xi}(-1)^{m/2} I_{m/2}(w),
\end{aligned} \tag{A.9}$$

where $I_\nu(z)$ is modified Bessel function, $\tilde{U}_{m_x,m_y}$ becomes[23]

$$\tilde{U}_{m_x,m_y} = \frac{C}{2\pi}\frac{\lambda r_0}{\gamma_{\mathrm{rel}}^3\beta_{\mathrm{rel}}^2}\int_0^\infty \mathrm{d}q \prod_{u=x,y} \frac{e^{-w_u} e^{im_u(\chi_u-\nu_u\theta)}(-1)^{m_u/2} I_{m_u/2}(w_u)}{\sqrt{2\sigma_u^2+q}} \qquad (m_u = \text{even}). \tag{A.10}$$

This means that the space charge potential makes only even-order resonances. Normalizing q with

$$\zeta = \frac{q}{\sigma_x^2+\sigma_y^2} + 1, \qquad \Delta_{xy} = -\Delta_{yx} = \frac{\sigma_x^2-\sigma_y^2}{\sigma_x^2+\sigma_y^2}, \tag{A.11}$$

$\tilde{U}_{m_x,m_y}, w_u$ becomes

$$\tilde{U}_{m_x,m_y} = \frac{C}{2\pi}\frac{\lambda r_0}{\gamma_{\mathrm{rel}}^3\beta_{\mathrm{rel}}^2}(-1)^{\frac{m_x+m_y}{2}} e^{im_x(\chi_x-\nu_x\theta)+im_y(\chi_y-\nu_y\theta)}\int_1^\infty \mathrm{d}\zeta \frac{e^{-w_x-w_y} I_{m_x/2}(w_x) I_{m_y/2}(w_y)}{\sqrt{\zeta^2-\Delta_{xy}^2}}, \tag{A.12}$$

$$w_u = \frac{J_u\beta_u}{(\sigma_x^2+\sigma_y^2)(\zeta+\Delta_{uv})} \qquad ((u,v) = (x,y),(y,x)). \tag{A.13}$$

Since the linear potential $\tilde{U}_{0,0}$ is

$$\tilde{U}_{0,0}(J_x,J_y;\theta) = \frac{C}{2\pi}\frac{\lambda r_0}{\gamma_{\mathrm{rel}}^3\beta_{\mathrm{rel}}^2}\int_1^\infty \mathrm{d}\zeta \frac{e^{-w_x-w_y} I_0(w_x) I_0(w_y)}{\sqrt{\zeta^2-\Delta_{xy}^2}}, \tag{A.14}$$

the modified phase due to the space charge effects is

$$\phi_u = \int_0^\theta (\nu_u + \frac{\partial\tilde{U}_{0,0}}{\partial J_u})\mathrm{d}\theta \tag{A.15}$$

$$= \nu_u\theta - \frac{\lambda r_0}{\gamma_{\mathrm{rel}}^3\beta_{\mathrm{rel}}^2}\int_0^s \mathrm{d}s \frac{\beta_u}{(\sigma_x^2+\sigma_y^2)}\int_1^\infty \mathrm{d}\zeta \frac{e^{-w_x-w_y}[I_0(w_u)-I_1(w_u)]I_0(w_v)}{(\zeta+\Delta_{uv})^{3/2}(\zeta+\Delta_{vu})^{1/2}}, \tag{A.16}$$

and the tune shift becomes

$$\Delta\nu_u = \frac{1}{2\pi}\oint \frac{\partial\tilde{U}_{0,0}}{\partial J_u}\mathrm{d}\theta \tag{A.17}$$

$$= -\frac{\lambda r_0}{\gamma_{\mathrm{rel}}^3\beta_{\mathrm{rel}}^2}\frac{1}{2\pi}\oint \mathrm{d}s \frac{\beta_u}{(\sigma_x^2+\sigma_y^2)}\int_1^\infty \mathrm{d}\zeta \frac{e^{-w_x-w_y}[I_0(w_u)-I_1(w_u)]I_0(w_v)}{(\zeta+\Delta_{uv})^{3/2}(\zeta+\Delta_{vu})^{1/2}}. \tag{A.18}$$

By introducing $\tau = 1/\zeta$, the tune shift can be written as a finite integral:

$$\Delta\nu_{u0} = -\frac{\lambda r_0}{\gamma_{\rm rel}^3\beta_{\rm rel}^2}\frac{1}{2\pi}\oint \mathrm{d}s\frac{\beta_u}{(\sigma_x^2+\sigma_y^2)}\int_0^1 \mathrm{d}\tau\frac{e^{-w_x-w_y}[I_0(w_u)-I_1(w_u)]I_0(w_v)}{(1+\Delta_{uv}\tau)^{3/2}(1+\Delta_{vu}\tau)^{1/2}} \tag{A.19}$$

$$w_u = \frac{J_u\beta_u\tau}{(\sigma_x^2+\sigma_y^2)(1+\Delta_{uv}\tau)}. \tag{A.20}$$

The second derivatives of the linear potential are

$$\oint \frac{\partial^2\tilde{U}_{0,0}}{\partial J_u^2}\mathrm{d}\theta = \frac{\partial\Delta\nu_u}{\partial J_u} \tag{A.21}$$

$$= \frac{\lambda r_0}{\gamma_{\rm rel}^3\beta_{\rm rel}^2}\frac{1}{2\pi}\oint \mathrm{d}s\frac{\beta_u^2}{(\sigma_x^2+\sigma_y^2)^2}\int_0^1 \mathrm{d}\tau\frac{e^{-w_x-w_y}[\frac{3}{2}I_0(w_u)-2I_1(w_u)+\frac{1}{2}I_2(w_u)]I_0(w_v)}{(1+\Delta_{uv}\tau)^{5/2}(1+\Delta_{vu}\tau)^{1/2}} \tag{A.22}$$

$$\oint \frac{\partial^2\tilde{U}_{0,0}}{\partial J_x\partial J_y}\mathrm{d}\theta = \frac{\partial\Delta\nu_x}{\partial J_y} = \frac{\partial\Delta\nu_y}{\partial J_x} \tag{A.23}$$

$$= \frac{\lambda r_0}{\gamma_{\rm rel}^3\beta_{\rm rel}^2}\frac{1}{2\pi}\oint \mathrm{d}s\frac{\beta_x\beta_y}{(\sigma_x^2+\sigma_y^2)^2}\int_0^1 \mathrm{d}\tau\prod_{(u,v)=(x,y),(y,x)}\frac{e^{-w_u}[I_0(w_u)-I_1(w_u)]}{(1+\Delta_{uv}\tau)^{3/2}}. \tag{A.24}$$

Expanding the nonlinear potential $\tilde{U}_{m_x,m_y}$ ($(m_x,m_y)\neq(0,0)$) with Fourier series of θ,

$$\tilde{U}_{m_x,m_y}(J_x,J_y;\theta) = \sum_n \hat{U}_{m_x,m_y,n}(J_x,J_y)e^{-in\theta}e^{-i\delta\theta} \qquad (\delta = m_x\nu_x+m_y\nu_y-n), \tag{A.25}$$

$$\hat{U}_{m_x,m_y,n} = \frac{\lambda r_0}{\gamma_{\rm rel}^3\beta_{\rm rel}^2}\frac{(-1)^{(m_x+m_y)/2}}{2\pi}\oint \mathrm{d}s e^{im_x\chi_x+im_y\chi_y}\int_0^\infty \mathrm{d}q\frac{e^{-w_x-w_y}I_{m_x/2}(w_x)I_{m_y/2}(w_y)}{\sqrt{2\sigma_x^2+q}\sqrt{2\sigma_y^2+q}} \tag{A.26}$$

$$= \frac{\lambda r_0}{\gamma_{\rm rel}^3\beta_{\rm rel}^2}\frac{(-1)^{(m_x+m_y)/2}}{2\pi}\oint \mathrm{d}s e^{im_x\chi_x+im_y\chi_y}\int_1^\infty \mathrm{d}\zeta\frac{e^{-w_x-w_y}I_{m_x/2}(w_x)I_{m_y/2}(w_y)}{\sqrt{\zeta^2-\Delta_{xy}^2}}. \tag{A.27}$$

Appendix B

Beam Tracking Code for Space Charge Simulation

In this chapter, the detailed explanations of the implementations of the Space Charge Tracker (SCTR)[42] is described.

SCTR employs the particle-in-cell algorithm to calculate the space charge potential. SCTR calculated transverse and vertical space charge forces separately. First, the beam distribution is projected onto a transverse mesh. The transverse space charge potentials are calculated to be satisfied with the two-dimensional Poisson equation. Then, the longitudinal distribution is assigned to the mesh, and the local line density is computed. Transverse and longitudinal kicks are calculated by the potential and the local line densities.

Table B.1: Typical parameters of SCTR for J-PARC MR

Parameter	Value
Particle number	200,000
Transverse mesh number	128×128
Transverse mesh size	$0.75^2 - 1.0^2$ mm^2
Longitudinal mesh number	128
Longitudinal mesh size	1 m
Intervals of space charge objects	1 - 2 m

The typical parameters for the space charge calculations are listed in Table B.1. These parameters can be easily changed in SCTR. The transverse beam emittance in MR is about 4.5π mm mrad for the neutrino user operation. Since the beta function in MR is $5 - 40$ m, the rms beam size is $4.7 - 14$ mm. It was verified that the space charge potential was distributed smoothly with the parameters in Table B.1. The small mesh size is suitable for the weak-intensity beam, which has small beam size. On the other hand, the mesh size must be large (or the number of mesh must be large) to an extent in discussing the beam loss. The transverse mesh size 0.75 mm corresponds to $2\pi J \sim 58\pi$ mm mrad at maximum beta. Considering that the typical parameters of the aperture of MR are 65π mm mrad (horizontal) and 63π mm mrad (vertical), the mesh size is small. The typical longitudinal beam size in MR is 50 m, which is large enough compared to the parameter in Table B.1.

To calculate the space charge potentials, the space charge objects are set in the ring. For the calculation of MR, the typical number of the space charge potentials is about 1000, corresponding to 1.6 m intervals.

Basically, the space charge potential is recalculated at every turn. However, sometimes it is effective to fix the space charge potential. We call this the "frozen model". In the frozen model, beams experience

the same space-charge-driven multipolar field effect at every turn. There are two merits for frozen medel simulations. One reason is that it can reflect clear effects of the space-charge-induced resonances. The other reason is that it can calculate faster than the basic mode.

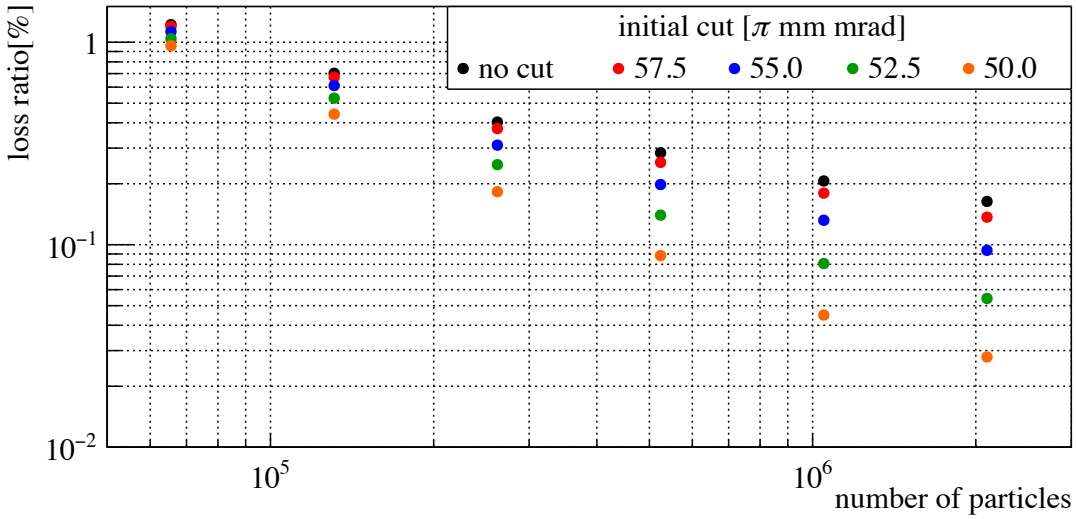

Figure B.1: The beam loss ratio as a function of the number of the macro particles. The simulation conditions are the same with those listed in Table 4. The beam optics is the "new optics" proposed in Chapter 3, 4. No errors were applied.

As written in Table B.1, the typical number of the macro particles used in the simulations is 200,000. It is expected that the motion of the beam core can be satisfactorily reproduced with this number. In fact, the turn-by-turn beam sizes were well reproduced in Chapter 2. However, in some ideal cases such as there are no errors and only a few particles are lost, it is difficult to reproduce the exact number of the lost particles. Figure B.1 shows the simulation results changing the number of the macro particles. The used optics is the "new optics" proposed in Chapter 3, 4. No errors were applied in the simulations. In this optics, the sextupole-driven resonance $\nu_x - 2\nu_y = -21$ is compensated (see Chapter 3), and the space-charge-induced resonances are weakened up to eighth order (see Chapter 4). The initial cuts were applied in transverse planes, since the beam was collimated in the transport line before injecting in MR. Comparing the data of the same cutting conditions, the larger the number of the macro particles was, the less the beam loss became. It shows that the beam was lost by the numerical errors. Moreover, in the real machine, there is the ambiguity for the initial cut. Further investigations are required to obtain the exact beam loss ratio.

Appendix C

Compensation of the Third-Order Nonstructure Resonances

Apert from structure resonances, nonstructure resonances are excited when there are unsymmetrical error sources. Though they are relatively weak compared to the structure resonances, their effects can not be neglected if they are near the setting tune.

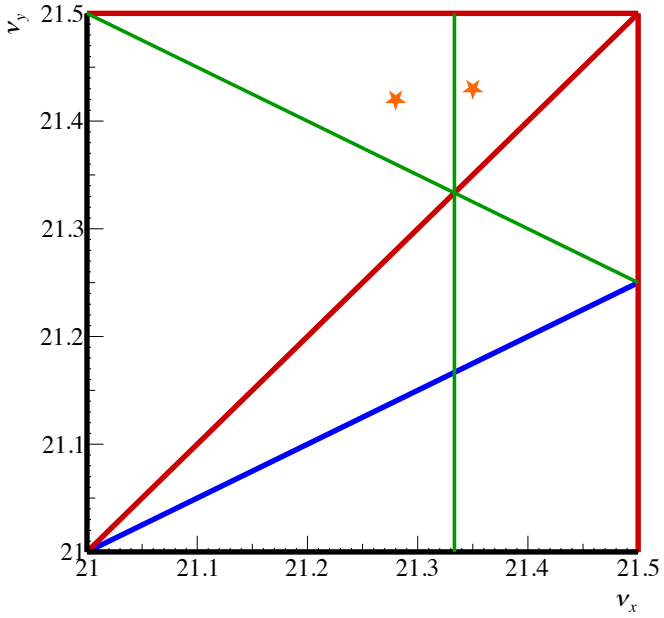

Figure C.1: Major resonances in J-PARC MR for the neutrino user operation. The black lines show the integer resonances, the red lines show the second-order resonances, the blue line show the third-order structure resonance, and the green lines show the third-order nonstructure resonances. The orange stars show the tunes where the trim coils of the sextupole magnets were scanned.

In J-PARC MR, the third-order nonstructure resonances have significant effects on the beam. Figure C.1 shows the major resonances for the neutrino user operation. The operation tune is $(\nu_x, \nu_y) = (21.35, 21.43)$. Since most of the tunes of the particles are distributed below the operation tune in both horizontal and vertical planes, the beam is affected by the third-order nonstructure resonances $3\nu_x = 64, \nu_x + 2\nu_y = 64$, shown as the green lines.

The driving term of the resonance is a vector quantity. Basically, one nonstructure resonance can be

compensated by two auxiliary magnets. Suppose the driving term $G_{3,0,64}$ of the resonance $3\nu_x = 64$ is compensated by the two auxiliary sextupole magnets at $s = s_A, s_B$. The strength of the auxiliary sextupole magnets should be set to meet the following condition:

$$\frac{\sqrt{2}}{24\pi}[\beta_{x,A}^{3/2}\Delta(K_2L)_A e^{i3\psi_{x,A}} + \beta_{x,B}^{3/2}\Delta(K_2L)_B e^{i3\psi_{x,B}}] + G_{3,0,64} = 0. \tag{C.1}$$

Here $\beta_{u,j}$ denotes the betatron function at $s = s_j$, $\Delta(K_2L)_j$ denotes the strength of the auxiliary sextupole magnet at $s = s_j$, and $\psi_{u,j}$ denotes the phase advance at $s = s_j$. In MR, four trim coils are installed at the sextupole magnets in total to compensate the two nonstructure resonances at the same time.

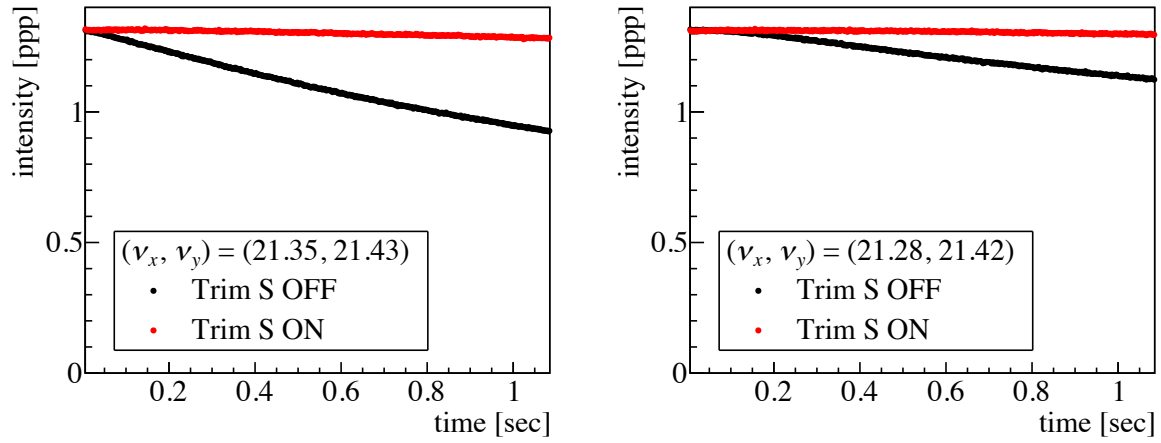

Figure C.2: Beam survival with and without trim coils at the sextupole magnets. The black lines show the beam survivals without using the trim coils, while the red lines show the results after the optimizations of the trim coils. The left picture shows the results at the tune $(\nu_x, \nu_y) = (21.35, 21.43)$, while the right picture shows the results at the tune $(\nu_x, \nu_y) = (21.28, 21.42)$. The beam intensities were measured by the DCCT.

Each resonance driving term is obtained by setting the tune on each resonance. The two trim coils are scanned to cancel the resonance driving term. The scan is performed by measuring the beam loss. When the beam is on the resonance, a lot of particles are lost due to the resonance. The trim coils are optimized to minimize the beam loss. Figure C.2 shows the examples of the scans, which were performed for the new optics proposed in Chapter 3, 4. Since the tune was shifted down by the space charge effects, the bare tune was not set exactly on the resonance. We searched for the setting tunes where the beam loss by the nonstructure resonances were large. The tunes were set at $(\nu_x, \nu_y) = (21.35, 21.43), (21.28, 21.42)$ for the measurements of the driving terms of the resonances $3\nu_x = 64, \nu_x + 2\nu_y = 64$, respectively. In both measurements, the beam survivals were recovered by applying the trim coils. The resonance driving terms $G_{3,0,64}, G_{1,2,64}$ were calculated by referring to the currents of the trim coils used in these optimizations.

In the present optics, the resonance driving terms were

$$G_{3,0,64} = 0.076e^{-0.70i}, \qquad G_{1,2,64} = 0.153e^{0.89i}, \tag{C.2}$$

while in the new optics,

$$G_{3,0,64} = 0.093e^{-0.63i}, \qquad G_{1,2,64} = 0.140e^{2.22i}. \tag{C.3}$$

If we very roughly assume that there was one strong source of the nonstructure resonances, the differences of the absolute values show the differences of the betatron functions, and the differences of the phases

terms show the differences of the phase advances. For both resonances, the absolute values of the driving terms are not so different. They can be explained by the differences of the betatron functions. The difference of the phase term in $G_{3,0,64}$ was small, while that in $G_{1,2,64}$ was large. This was explained by the fact that the apparent difference between the present optics and the new optics was the vertical phase advances.

To compensate the two resonances at the same time, the strength of the four auxiliary sextupole magnets, which are located at $s = s_A, s_B, s_C, s_D$, should be set to meet the following conditions:

$$\frac{\sqrt{2}}{24\pi} \sum_{j=A,B,C,D} [\beta_{x,j}^{3/2} \Delta(K_2 L)_j e^{i3\psi_{x,j}}] + G_{3,0,64} = 0, \tag{C.4}$$

$$\frac{\sqrt{2}}{8\pi} \sum_{j=A,B,C,D} [\beta_{x,j}^{1/2} \beta_{y,j} \Delta(K_2 L)_j e^{i(\psi_{x,j}+2\psi_{y,j})}] + G_{1,2,64} = 0. \tag{C.5}$$

These equations can be solved as

$$\begin{pmatrix} \Delta(K_2L)_A \\ \Delta(K_2L)_B \\ \Delta(K_2L)_C \\ \Delta(K_2L)_D \end{pmatrix} = -\frac{8\pi}{\sqrt{2}} (\boldsymbol{V}_A, \boldsymbol{V}_B, \boldsymbol{V}_C, \boldsymbol{V}_D)^{-1} \begin{pmatrix} 3\mathrm{Re}[G_{3,0,64}] \\ 3\mathrm{Im}[G_{3,0,64}] \\ \mathrm{Re}[G_{1,2,64}] \\ \mathrm{Im}[G_{1,2,64}] \end{pmatrix}, \tag{C.6}$$

$$\boldsymbol{V}_j = \begin{pmatrix} \beta_{x,j}^{3/2} \cos(3\psi_{x,j}) \\ \beta_{x,j}^{3/2} \sin(3\psi_{x,j}) \\ \beta_{x,j}^{1/2} \beta_{y,j} \cos(\psi_{x,j} + 2\psi_{y,j}) \\ \beta_{x,j}^{1/2} \beta_{y,j} \sin(\psi_{x,j} + 2\psi_{y,j}) \end{pmatrix}. \tag{C.7}$$

Of course, the matrix $(\boldsymbol{V}_A, \boldsymbol{V}_B, \boldsymbol{V}_C, \boldsymbol{V}_D)$ should be regular.

After applying the calculated values, all trim coils are scanned and fine optimized in the experiment. In many cases, the values obtained by the Eq. (C.6) are not the best. One reason is that in measuring the resonance driving term $G_{3,0,64}$, the beam is affected not only by $3\nu_x = 64$, but also by $\nu_x + 2\nu_y = 64$. In short, there were some systematic errors in the driving term $G_{3,0,64}$. Another possible reason is that the calibrations of the trim coils might be not perfect. The systematic errors of the phase advances in the calculations may also be the reason. Strictly, the resonance driving term obtained by changing the bare tune and that by considering the detuning is different. If this is the main reason, fine tuning is inevitable, because the incoherent detuning can not be measured. Further studies are required to understand the phenomenon.

The present method uses the beam loss for the evaluation of the resonance driving terms, which makes it difficult to specify the resonance. In principle, the resonance driving terms can be separately evaluated by measuring the resonant spectra (see Section 3). The issue of this method is the noise. The resonant spectra of the third-order nonstructure resonances are almost at the noise level. To realize this method, improvement of the signal to noise ratio of the BPM is essential.

Appendix D

Potentials of the Space-Charge-Induced Structure Resonances

In this chapter, the potentials of the space-charge-induced structure resonances are listed. The most influential resonance was $8\nu_y = 171$ at the tune $(\nu_x, \nu_y) = (21.34, 21.44)$. Comparing these figures with the result of the beam loss (Fig. 4), it is clear the other resonances were not the main sources of the beam loss. However, the influential resonance will be changed if the tune is moved. If you move the tune down and to the right, you may have to care for the fourth-order resonance $2\nu_x - 2\nu_y = 0$. If you move the tune to the left, you may have to care for the sixth-order resonance $4\nu_x - 2\nu_y = 42$. If you move the tune up and to the right, the most influential tune may be changed to the resonance $2\nu_x + 6\nu_y = 171$. The proper vertical phase advance in the arc section $\Delta\psi_{\mathrm{arc},y}$ should be employed, considering which is the most influential resonance.

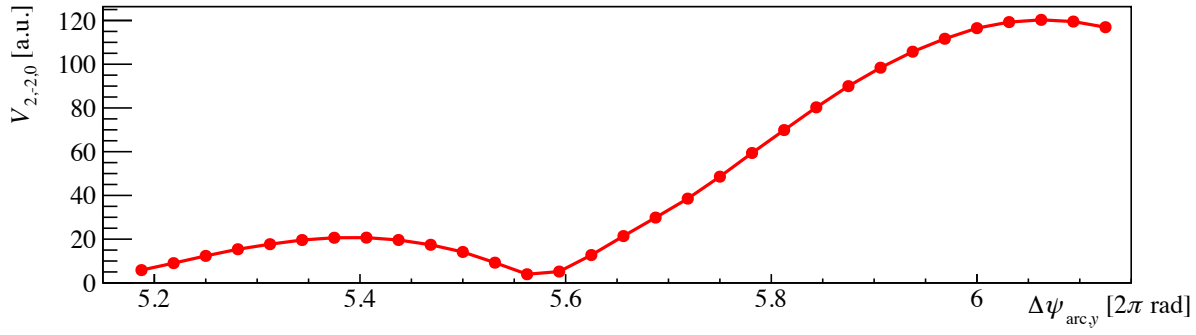

Figure D.1: Potentials of the resonance $2\nu_x - 2\nu_y = 0$.

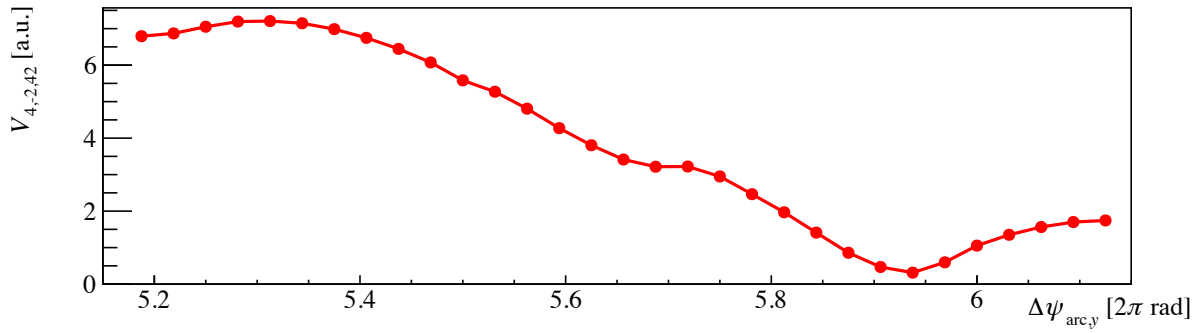

Figure D.2: Potentials of the resonance $4\nu_x - 2\nu_y = 42$.

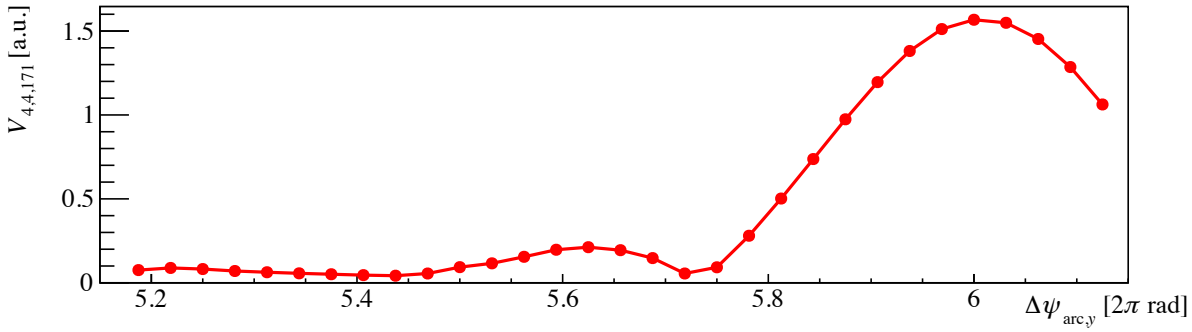

Figure D.3: Potentials of the resonance $4\nu_x + 4\nu_y = 171$.

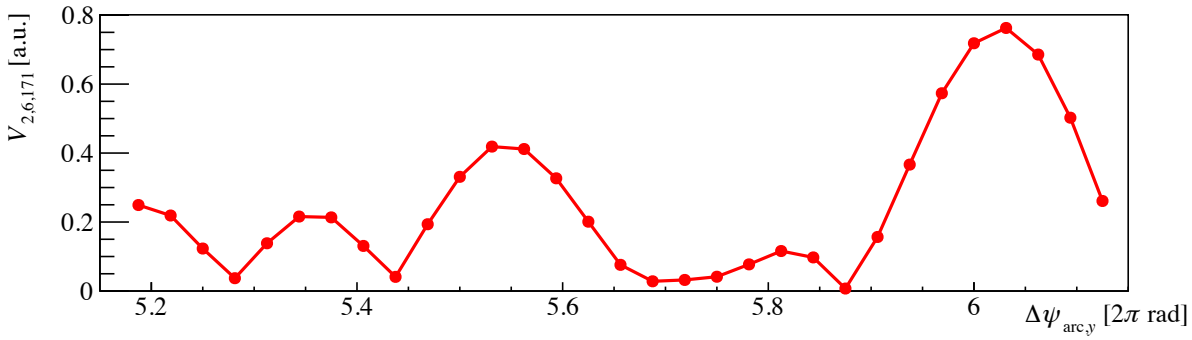

Figure D.4: Potentials of the resonance $2\nu_x + 6\nu_y = 171$.

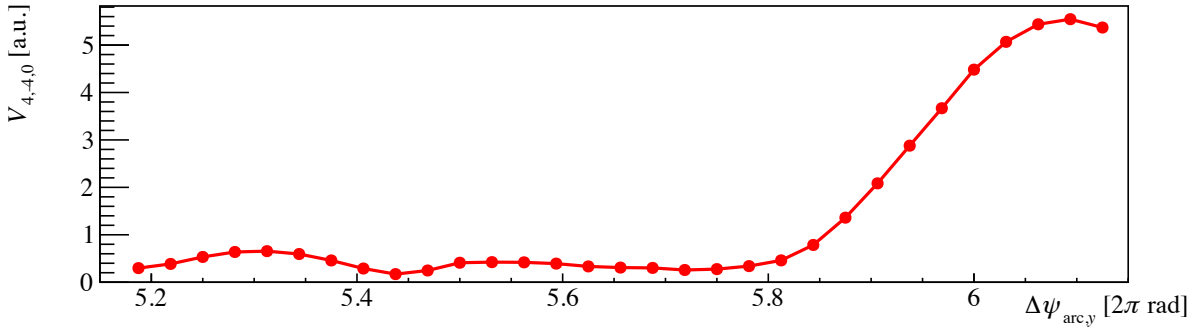

Figure D.5: Potentials of the resonance $4\nu_x - 4\nu_y = 0$.

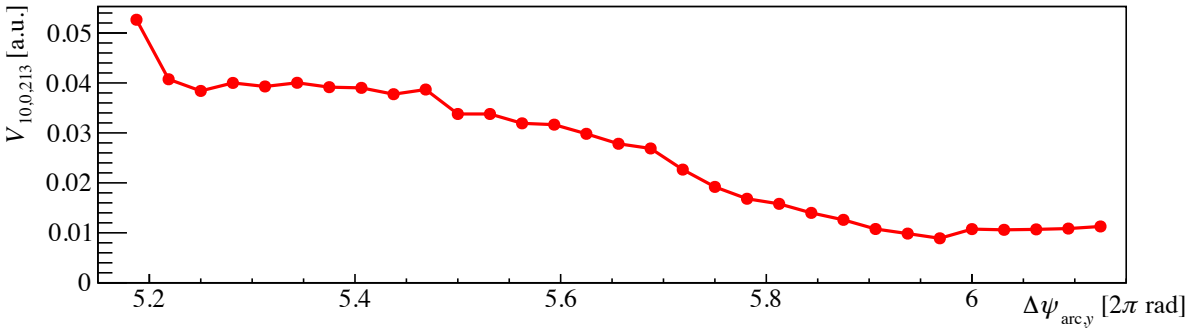

Figure D.6: Potentials of the resonance $10\nu_x = 213$.

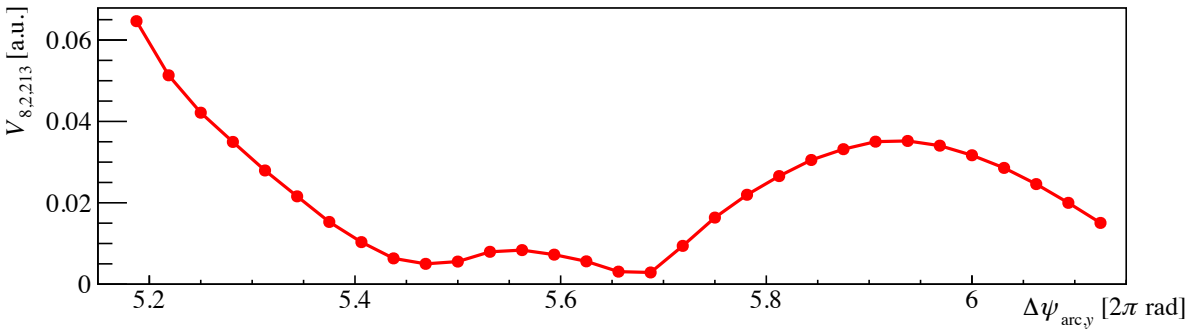

Figure D.7: Potentials of the resonance $8\nu_x + 2\nu_y = 213$.

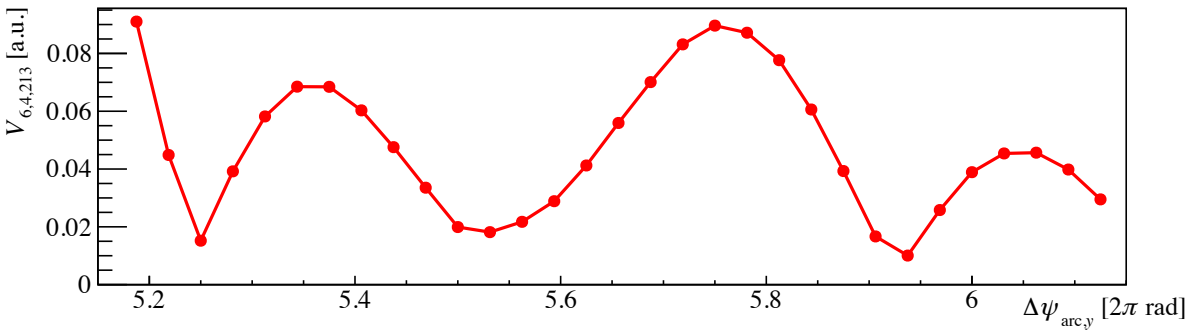

Figure D.8: Potentials of the resonance $6\nu_x + 4\nu_y = 213$.

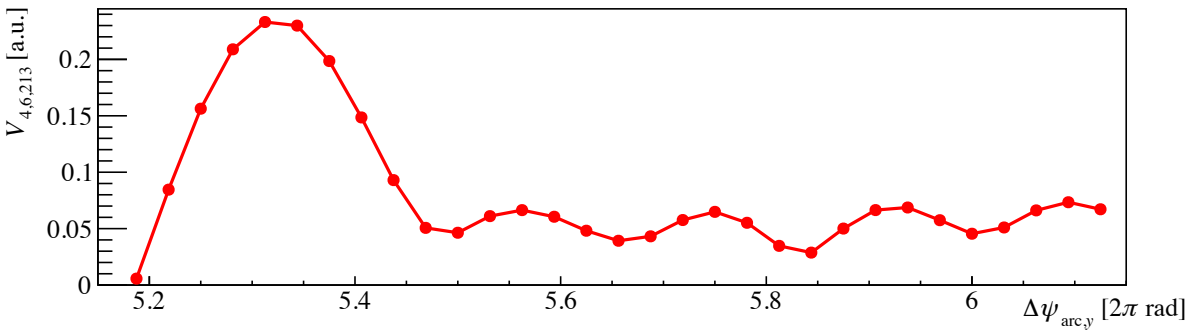

Figure D.9: Potentials of the resonance $4\nu_x + 6\nu_y = 213$.

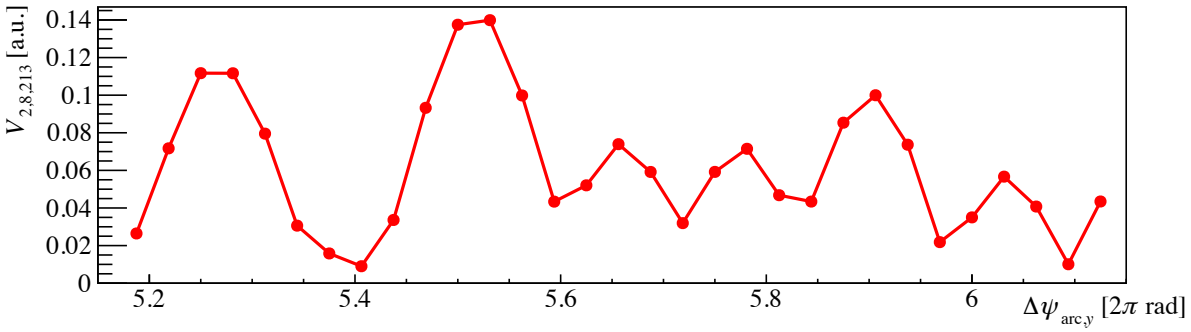

Figure D.10: Potentials of the resonance $2\nu_x + 8\nu_y = 213$.

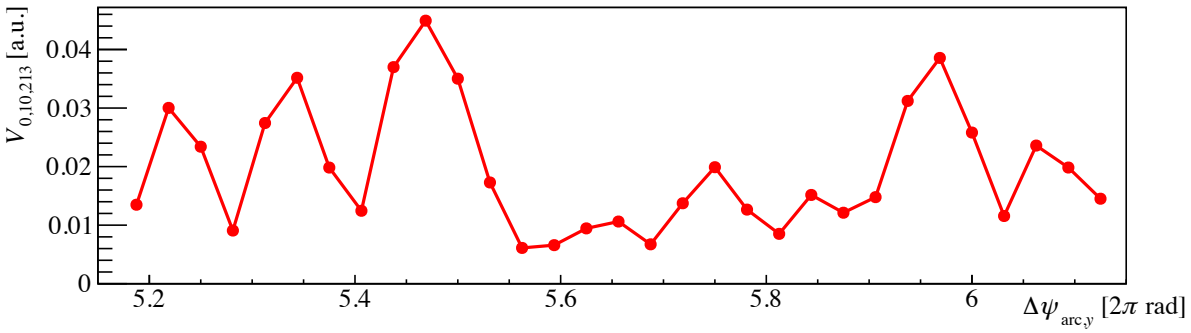

Figure D.11: Potentials of the resonance $10\nu_y = 213$.

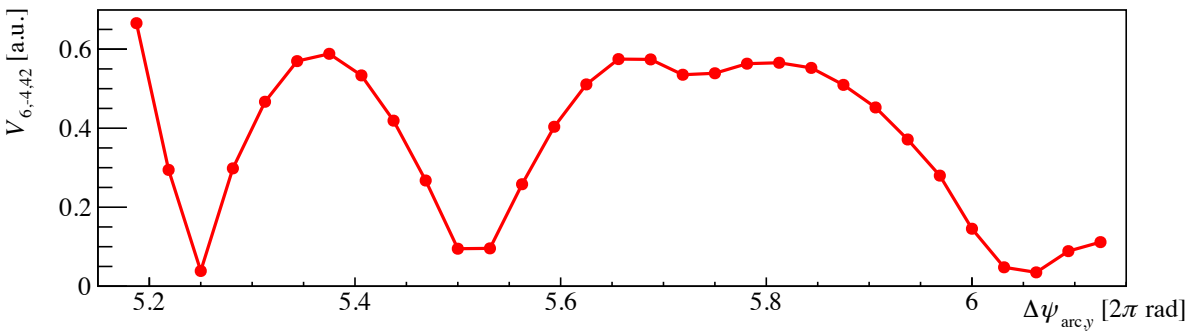

Figure D.12: Potentials of the resonance $6\nu_x - 4\nu_y = 42$.

Bibliography

[1] M. L. Oliphant, "The acceleration of particles to very high energies", Classified memo submitted to DSIR (1943), University of Birmingham Archive.

[2] V. I. Veksler, "A new method of accelerating relativistic particles," The Proceedings of the USSR Academy of Sciences **43**, 8 (1944), pp. 329–331, http://lhe.jinr.ru/rus/veksler/wv0/publikacii/1944Veksler.pdf, in Russian.

[3] E. M. McMillan, "The synchrotron – A proposed high energy particle accelerator", Phys. Rev. **68**, 143 (1945).

[4] N. C. Christofilos, "Focussing system for ions and electrons", US patent 2736799, filed 1950-03-10, issued 1956-02-28.

[5] E. D. Courant, M. S. Livingston, and H. S. Snyder, "The strong-focusing synchroton – A new high energy accelerator", Phys. Rev. **88**, 1190 (1952).

[6] T. Kitagaki, "A focusing method for large accelerators", Phys. Rev. **89**, 1161 (1953).

[7] E. D. Courant and H. S. Snyder, "Theory of the alternating-gradient synchrotron", Annals of Physics **3**, 1 (1958).

[8] A. Schoch, "Theory of linear and non-linear perturbations of betatron oscillations in alternating gradient synchrotrons", Technical Report CERN 57–23, (CERN, Geneva, 1957), doi:10.5170/CERN-1957-021.

[9] G. Guignard, "The general theory of all sum and difference resonances in a three-dimensional magnetic field in a synchrotron", Technical Report CERN 76–06, (CERN, Geneva, 1976), doi:10.5170/CERN-1976-006.

[10] L. C. Teng, "Transverse space charge effects", ANLAD-59, Argonne National Laboratory, February 1 (1960), https://lss.fnal.gov/archive/other/anlad-59.pdf.

[11] L. J. Laslett, "On intensity limitations imposed by transverse space-charge effects in circular particle accelerators", in *Proc. 1963 Summer Study on Storage Rings, Accelerators and Experimentation at Super-High Energies, NY, USA, June 1963*, pp. 324–367, https://lss.fnal.gov/conf/C630610/p324.pdf.

[12] S. Machida, "Space-charge-induced resonances in a synchrotron", Nucl. Instrum. Methods Phys. Res., Sect. A **384**, 316 (1997).

[13] T. Koseki *et al.*, "Beam commissioning and operation of the J-PARC main ring synchrotron", Prog. Theor. Exp. Phys. **2012**, 02B004 (2012).

[14] High-intensity Proton Accelerator Project Team, "Accelerator technical design report for high-intensity proton accelerator facility project, J-PARC", KEK-Report 2002-13 and JAERI-TECH 2003-044 (2003), https://jopss.jaea.go.jp/pdfdata/JAERI-Tech-2003-044.pdf.

[15] M. Yoshii *et al.*, "Present status of J-PARC ring rf systems", in *Proc. PAC' 07, Albuquerque, New Mexico, June 2007*, (JACoW Publishing, Geneva, Switzerland, 2016), pp. 1511–1513, http://accelconf.web.cern.ch/p07/PAPERS/TUPAN055.PDF.

[16] C. Ohmori *et al.*, "Development of a high gradient rf system using a nanocrystalline soft magnetic alloy", Phys. Rev. ST Accel. Beams **16**, 112002 (2013).

[17] S. Igarashi, "High-power beam operation at J-PARC", in *Proc. HB' 18, Daejeon, Korea, June 2018*, (JACoW Publishing, Geneva, Switzerland, 2018), pp. 147–152, doi:10.18429/JACoW-HB2018-TUA2WD02.

[18] S. Igarashi *et al.*, "Accelerator design for 1.3 MW beam power operation of the J-PARC main ring", submitted to Prog. Theor. Exp. Phys.

[19] J. Wei, "Rare isotope beams and high-power accelerators", in *Proc. NAPAC'19, Lansing, Michigan, USA, September 2019*, (JACoW Publishing, Geneva, Switzerland, 2020), pp. 993–999, doi:10.18429/JACoW-NAPAC2019-FRXBB1.

[20] E. Pozdeyev, "Status of the PIP-II project at FNAL", 4th ICFA Mini-Workshop on Space Charge 2019, November 2019, https://cds.cern.ch/record/2698493.

[21] T. Yasui, S. Igarashi, Y. Sato, T. Koseki, and K. Ohmi, "Transverse emittance growth caused by space-charge-induced resonance", Phys. Rev. Accel. Beams **23**, 061001 (2020).

[22] J. L. Tennyson, "The dynamics of the beam-beam interaction", in *AIP Conf. Proc. No. 87*, 345 (1982), doi:10.1063/1.33618.

[23] K. Ohmi and K. G. Sonnad, "Beta function measurement and resonances induced by space charge force and lattice magnets", in *Proc. IPAC' 16, Busan, Korea, May 2016*, (JACoW Publishing, Geneva, Switzerland, 2016), pp 641–643, doi:10.18429/JACoW-IPAC2016-MOPOR019.

[24] S. Kheifets, "Potential of a three-dimensional Gaussian bunch", PETRA Note 119 (1976), doi:10.3204/PUBDB-2017-01789.

[25] F. J. Sacherer, "Transverse space-charge effects in circular accelerators", Ph.D. thesis, University of California, Berkeley, 1968, https://escholarship.org/uc/item/9037d511.

[26] J-PARC center, pamphlet, https://j-parc.jp/documents/pamphlet/J-PARC201708.pdf, in Japanese.

[27] 内藤富士雄, 「J-PARC 加速器の概要」, OHO'18 テキスト, 2018 年, http://accwww2.kek.jp/oho/OHOtxt/OHO-2018/01_Naito%20_Fujio_181004.pdf, in Japanese.

[28] H. Hotchi *et al.*, "Beam commissioning of the 3-GeV rapid cycling synchrotron of the Japan Proton Accelerator Research Complex", Phys. Rev. ST Accel. Beams **12**, 040402 (2009).

[29] Y. Fukuda *et al.* (Super-Kamiokande Collaboration), "Evidence for oscillation of atmospheric neutrinos", Phys. Rev. Lett. **81**, 1562 (1998).

[30] K. Abe *et al.* (T2K Collaboration), "Indication of electron neutrino appearance from an accelerator-produced off-axis muon neutrino beam", Phys. Rev. Lett. **107**, 041801 (2011).

[31] K. Abe *et al.* (T2K Collaboration), "Observation of electron neutrino appearance in a muon neutrino beam", Phys. Rev. Lett. **112**, 061802 (2014).

[32] The T2K Collaboration, "Constraint on the matter-antimatter symmetry-violating phase in neutrino oscillations", Nature **580**, 339–344 (2020).

[33] Y. Hashimoto, S. Hiramatsu, D. Arakawa, M. Arinaga, M. Tejima, and T. Toyama, "Characteristics of a DCCT for the J-PARC main ring", in *Proc. PASJ'08, Tsukuba, Japan, August 2011*, pp. 451–455, https://www.pasj.jp/web_publish/pasj8/proceedings/poster/MOPS064.pdf, in Japanese.

[34] T. Toyama, Y. Hashimoto, Y. Sato, M. Tejima, and S. Yamada, "Beam-based correction of a DCCT response", in *Proc. PASJ'08, Tsukuba, Japan, August 2011*, pp. 465–467, https://www.pasj.jp/web_publish/pasj8/proceedings/poster/MOPS068.pdf, in Japanese.

[35] Y. Omori, Y. Hashimoto, T. Toyama, and S. Otsu, "A calibration method for beam DCCT of J-PARC main ring", in *Proc. PASJ'08, Tsukuba, Japan, August 2011*, pp. 456–459, https://www.pasj.jp/web_publish/pasj8/proceedings/poster/MOPS065.pdf, in Japanese.

[36] K. Satou, T. Toyama, and M. Tejima, "Present performance of a DCCT for J-PARC MR", in *Proc. PASJ'13, Chiba, Japan, August 2016*, pp. 1076–1080, https://www.pasj.jp/web_publish/pasj2016/proceedings/PDF/TUP0/TUP076.pdf, in Japanese.

[37] K. Satou, T. Toyama, Y. Hashimoto, M. Tejima, S. Lee, and K. Yamamoto, "Present status of the J-PARC MR BLM system", in *Proc. PASJ' 06, Tokai, Japan, August 2009*, pp. 295–297, https://www.pasj.jp/web_publish/pasj6/papers/wpbda05.pdf, in Japanese.

[38] K. Satou and T. Toyama, "Upgrade scheme of BLM system of J-PARC MR", in *Proc. PASJ' 08, Tsukuba, Japan, August 2011*, pp. 424–428, https://www.pasj.jp/web_publish/pasj8/proceedings/poster/MOPS058.pdf, in Japanese.

[39] K. Satou, N. Kamikubota, T. Toyama, S. Yamada, and S. Yoshida, "Development of wide dynamic range beam loss monitor system for the J-PARC main ring", in *Proc. IPAC'17, Copenhagen, Denmark, May 2017*, (JACoW Publishing, Geneva, Switzerland, 2017), pp. 1248–1251, doi:10.18429/JACoW-IPAC2017-TUOAB3.

[40] Y. Sato *et al.*, "Recent commissioning and prospect of high power beam operation of the J-PARC main ring", in *Proc. PASJ'12, Tsuruga, Japan, August 2015*, pp. 488–492, https://www.pasj.jp/web_publish/pasj2015/proceedings/PDF/WEP0/WEP031.pdf, in Japanese.

[41] Y. Sato, "High power beam operation of the J-PARC RCS and MR", in *Proc. IPAC'18, Vancouver, BC, Canada, May 2018*, (JACoW Publishing, Geneva, Switzerland, 2018), pp. 2938–2942, doi:10.18429/JACoW-IPAC2018-THYGBF1.

[42] K. Ohmi, S. Igarashi, H. Koiso, T. Koseki, and K. Oide, "Study of halo formation in J-PARC MR", in *Proc. PAC'07, Albuquerque, NM, USA, June 2007*, (IEEE, New York, 2007), pp. 3318–3320, http://accelconf.web.cern.ch/p07/PAPERS/THPAN040.PDF.

[43] K. Ohmi, "Artificial noise in PIC codes and consequences on long term tracking", in *Proc. HB'14, East-Lansing, MI, USA, November 2014*, (JACoW Publishing, Geneva, Switzerland, 2015), pp. 259–266, http://accelconf.web.cern.ch/HB2014/papers/weo2lr03.pdf.

[44] A. Kobayashi, S. Igarashi, Y. Sato, T. Shimogawa, Y. Sugiyama, T. Toyama, and M. Yoshii, "Studies on coherent multi-bunch tune shift with different bunch spacing at the J-PARC main ring", in *Proc. IPAC'19, Melbourne, Australia, May 2019*, (JACoW Publishing, Geneva, Switzerland, 2019), pp. 167–170, doi:10.18429/JACoW-IPAC2019-MOPGW036.

[45] Y. Hashimoto *et al.*, "Multi-wire beam profile monitor for J-PARC 3-50 BT and MR", in *Proc. PASJ'05, Higashihiroshima, Japan, August 2008*, pp. 310–312, https://www.pasj.jp/web_publish/pasj5_lam33/contents/PDF/WP/WP021.pdf, in Japanese.

[46] Y. Hashimoto *et al.*, "Multi-ribbon profile monitor using carbon graphite foil for J-PARC", in *Proc. HB'10, Morschach, Switzerland, 2010*, pp. 429–433, http://accelconf.web.cern.ch/HB2010/papers/weo2a01.pdf.

[47] H. Akino, Y. Hashimoto, M. Mitani, S. Otsu, Y. Omori, Y. Takiyama, and T. Toyama, "New multi-ribbon beam profile monitor with titanium foil of 1.2 microns for intense proton beam in the J-PARC", in *Proc. PASJ'11, Aomori, Japan, August 2014*, pp. 1221–1225, https://www.pasj.jp/web_publish/pasj2014/proceedings/PDF/SUP0/SUP081.pdf, in Japanese.

[48] M. Tanabashi *et al.* (Particle Data Group), "Review of particle physics", Phys. Rev. D **98**, 030001, (2018).

[49] SAD home page.

[50] S. Igarashi, K. Ishii, T. Koseki, A. Molodozhentsev, K. Niki, K. Okamura, M. Tomizawa, and E. Yanaoka, "Study of the J-PARC MR beam orbit based on the magnetic field measurements", in *Proc. PASJ'07, Wako, Japan, August 2007*, pp. 601–603, https://www.pasj.jp/web_publish/pasj4_lam32/PASJ4-LAM32/contents/PDF/TP/TP62.pdf.

[51] T. Toyama, D. Arakawa, Y. Hashimoto, S. Lee, T. Miura, S. Muto, N. Hayashi, R. Toyokawa, and J. Kishiro, "Beam diagnostics for the J-PARC main ring synchrotron", in *Proc. PAC'05, Knoxville, Tennessee, USA, May 2005*, (IEEE, Piscataway, NJ, 2005), pp. 958–960, http://accelconf.web.cern.ch/p05/PAPERS/RPAT005.PDF.

[52] Y. S. Tsai, "Pair production and bremsstrahlung of charged leptons", Rev. Mod. Phys. **46**, 815 (1974).

[53] S. Y. Lee, "Accelerator physics", Fourth edition, (World Scientific, Singapore, 2019), doi:10.1142/11111.

[54] K. Nakamura and Y. Kurimoto, "Measurement betatron amplitude function during acceleration in J-PARC main ring", in *Proc. PASJ'12, Tsuruga, Japan, August 2015*, pp. 958–962, https://www.pasj.jp/web_publish/pasj2015/proceedings/PDF/THP0/THP016.pdf, in Japanese.

[55] T. Toyama, D. Arakawa, R. Toyokawa, A. Nakamura, N. Hayashi, and T. Miura, 「J-PARC 50 GeV Ring の BPM 検出器」, in *Proc. SAST'03, Tsukuba, Japan, November 2003*, 2P-021(S-291), http://conference.kek.jp/sast03it/WebPDF/2P021.pdf, in Japanese.

[56] T. Toyama *et al.*, "Beam diagnostics in J-PARC MR commissioning", in *Proc. PASJ'05, Higashihiroshima, Japan, August 2008*, pp. 298–300, https://www.pasj.jp/web_publish/pasj5_lam33/contents/PDF/WP/WP017.pdf, in Japanese.

[57] K. Satou *et al.*, "Beam diagnostic system of the main ring synchrotron of J-PARC", in *Proc. HB'08, Nashville, Tennessee, USA, 2008*, pp. 472–474, http://accelconf.web.cern.ch/HB2008/papers/wgf11.pdf.

[58] T. Toyama *et al.*, "Beam diagnostics at the first beam commissioning of the J-PARC MR", in *Proc. PAC'09, Vancouver, BC, Canada, June 2007*, (JACoW Publishing, Geneva, Switzerland, 2009), pp. 1964–1966, http://accelconf.web.cern.ch/PAC2009/papers/we4grc01.pdf.

[59] T. Toyama, Y. Hashimoto, K. Hanamura, S. Hatakeyama, M. Okada, and M. Tejima, "Performance and upgrade of BPMs at the J-PARC MR", in *Proc. IBIC'12, Tsukuba, Japan, October 2012*, (JACoW Publishing, Geneva, Switzerland, 2012), pp. 107–111, http://accelconf.web.cern.ch/IBIC2012/papers/mopa26.pdf.

[60] J. Laskar, C. Froeschlé, and A. Celletti, "The measure of chaos by the numerical analysis of the fundamental frequencies. Application to the standard mapping", Physica (Amsterdam) **56D**, 253 (1992).

[61] J. Laskar, "Introduction to frequency map analysis", in *Proc. NATO ASI, "Hamiltonian Systems with Three or More Degrees of Freedom", C. Simó (ed.), S'Agaro, Spain, June 1995*, Kluwer, pp. 134–150 (1999), doi:10.1007/978-94-011-4673-9_13.

[62] M. G. Minty and F. Zimmermann, "Measurement and control of charged particle beams", (Springer, Berlin, 2003), doi:10.1007/978-3-662-08581-3.

[63] R. Bartolini and F. Schmidt, "Normal form via tracking or beam data", Part. Accel. **59**, 93 (1998), https://cds.cern.ch/record/333077.

[64] A. Franchi, R. Tomás, and F. Schmidt, "Magnet strength measurement in circular accelerators from beam position monitor data", Phys. Rev. ST Accel. Beams **10**, 074001, (2007).

[65] H. Okamoto and K. Yokoya, "Parametric resonances in intense one-dimensional beams propagating through a periodic focusing channel", Nucl. Instrum. Methods Phys. Res., Sect. A **482**, 51 (2002).

[66] K. Ito, H. Okamoto, Y. Tokashiki, and K. Fukushima, "Coherent resonance stop bands in alternating gradient beam transport", Phys. Rev. Accel. Beams **20**, 064201 (2017).

[67] H. Hotchi, Y. Watanabe, H. Harada, K. Okabe, P. K. Saha, Y. Shobuda, F. Tamura, and M. Yoshimoto, "Pulse-by-pulse switching of operational parameters in J-PARC 3-GeV RCS", J. Phys. Conf. Ser. **1067**, 052015 (2018).